

High-resolution temperature profiling in the Π Chamber: variability of statistical properties of temperature fluctuations

Robert Grosz¹, Kamal Kant Chandrakar², Raymond A. Shaw³, Jesse C. Anderson³, Will Cantrell³, and Szymon P. Malinowski¹

¹Institute of Geophysics, Faculty of Physics, University of Warsaw, Pasteura 5, 02-293 Warsaw, Poland

²Mesoscale & Microscale Meteorology Laboratory, NSF National Center for Atmospheric Research, 3090 Center Green Drive, Boulder, CO 80301, USA

³Department of Physics, Michigan Technological University, 1400 Townsend Drive, Houghton, MI 49931, USA

Correspondence: Robert Grosz (rgrosz@fuw.edu.pl)

Abstract.

This study delves into the small-scale temperature structure of Rayleigh-Bénard convection (RBC) generated in the Π Chamber under three temperature differences (10 K, 15 K, and 20 K) at Rayleigh number $\text{Ra} \sim 10^9$ and Prandtl number $\text{Pr} \approx 0.7$. We performed high resolution frequency measurements (2 kHz) with the UltraFast Thermometer (UFT) at selected points

5 along the vertical axis to explore to what extent the Π Chamber can be described as an idealized RBC flow. The miniaturized design of the sensor featured with a resistive platinum-coated tungsten wire, 2.5 μm thick and 3 mm long, mounted on a miniature wire probe allowed for undisturbed vertical temperature profiling vertically undisturbed temperature profiling through the chamber's depth spanning from 8 cm above the bottom surface to 5 cm below the top surface. The resulting rich dataset comprised both long (The collected data, consisting of 19 min) and short (and 3 min) time series, revealing significant were
10 used to investigate the variability of the temperature field within the chamber, aiming to better address scientific questions related to its primary objective—small-scale aerosol-cloud interactions. The analyses reveal substantial variability in both variance and skewness variability in the of temperature distributions near both surfaces and the top and bottom plates and in the bulk (central) region linked with, which were linked to local thermal plume dynamics. We also identified three spectral regimes termed inertial range (slopes of $\sim -7/5$), transition range (slopes of ~ -3) and dissipative range, characterized by
15 slopes varying ~ -7 . Furthermore, the analysis showed a robust power law relationship between the periodicity of large-scale circulation (LSC) and the temperature difference, describable by an exponential relation. Notably, the experimental findings demonstrate strong experimental results are in good agreement with Direct Numerical Simulations (DNS) conducted under similar thermodynamic conditions, illustrating a rare comparative analysis of this nature.

1 Introduction

20 The convection-cloud chamber, officially named the Π Chamber, represents one of the most advanced facilities for controlled experiments on cloud microphysics (Chang et al., 2016). Its design allows for reproducible and controlled measurements across a wide range of temporal scales, from minutes to days, while maintaining stationary thermodynamic forcing. It operates in two

modes. The first mode utilizes static pressure reduction to simulate updrafts in the atmosphere. In the second mode, it induces Rayleigh-Bénard convection, where air in the chamber is heated from below and cooled from above. In the present study we 25 investigate temperature fluctuations in full spectrum of scales in the chamber operating in the second mode. We focus on small-scale temperature fluctuations in a course of turbulent mixing inside the chamber, since the facility is designed for research on aerosol-cloud interactions in ~~a~~turbulent environment (Chandrakar et al., 2018a, b; Desai et al., 2018, 2019; Chandrakar et al., 2020; Prabhakaran et al., 2020; MacMillan et al., 2022). Unlike typical RBC experiments, the chamber includes side windows and various mounting points for microphysical instrumentation, which introduce asymmetries between the upper and lower 30 plates. Thus the detailed (e.g. thermal) characterization of the chamber is required to evaluate how closely the flow resembles classic RBC flows. It is important to note that this study does not aim to extend beyond conventional RBC research, which often involves day-long averaging. Nonetheless, we report ~~very~~ rich statistics compared to previous highly-resolved measurements within the thermal boundary layer of RBC~~RBC~~ systems (du Puits et al., 2013; du Puits, 2022; du Puits, 2024).

Our work primarily focuses on understanding the small-scale and short-term variability of thermal conditions within the 35 facility, emphasizing the importance of absolute temperature. This aspect is crucial for more comprehensive studies on aerosol interactions with water vapor and droplet growth/evaporation in a turbulent environment. However, a few selected results are presented in a non-dimensional form (see Appendix B). Worth highlighting paper ~~is in~~ terms of small-scale variability is the a recent work on the subgrid scale scalar variance modeled in large eddy simulations ~~for over the range~~ $\text{Ra} \sim 10^8\text{--}10^9$ (Salesky et al., 2024). Our approach was to collect high resolution (2 kHz) temperature time series using the UltraFast Thermometer 40 (UFT) at selected locations in a vertical profile near the axis of the chamber and to perform statistical and spectral analysis investigating small-scale structure of RBC under laboratory conditions.

UltraFast Thermometers (UFTs) have been specifically designed for airborne in-cloud measurements, ~~achieving resolutions down to scales within and~~. They resolve scales down to or even below 1 cm, effectively reaching the dissipation range. Successive iterations~~models~~ of the UFT family (Haman et al., 1997, 2001; Kumala et al., 2013) have utilized similar sensing 45 element—a resistive platinum-coated tungsten wire, 2.5 μm thick and 5 mm long, mounted on a small vane to adapt to local airflow ~~dynamics~~. In the next sensor versions (Nowak et al., 2018; Siebert et al., 2021), the vane has been removed, leading to further miniaturization of the instrument's dimensions and the implementation of a custom-built electronic system. The current iteration (UFT-2B) has undergone testing i.e. during the recent EUREC⁴A campaign (Stevens et al., 2021). The 3 mm long sensing wire is spanned on an industry-standard miniature wire probe, allowing for easy exchange of the sensing head (see Fig. 50 1).

Not only small-scale fluctuations are important ~~but also in their own sake, but also for~~ understanding of changes in the LSC on distributions of mixing ratio, temperature, and supersaturation inside the cell. The established LSC period in the II Chamber at the temperature difference of 12 K, was ~~approximated to estimated to be~~ $\tau_{12} \approx 72$ s (moist convection characterized by a mixing ratio of 7.55 g kg^{-1}) (Anderson et al., 2021). In this paper we investigate LSC for three temperature differences (ΔT): 55 10 K, 15 K, and 20 K showing a variability of periodicity which can be described by the ~~exponential~~power law function.

Over the years, numerous attempts have been made to characterize the statistical aspects of thermal convection in convective cells~~RBC~~ chambers. Comprehensive overviews of recent advancements in natural convection are provided by Fan et al. (2021)



Figure 1. UFT-2B head sensor. A parallel to the mean flow, tungsten wire (2.5 μm thick, 3 mm long) spanned on miniature industry-standard wire probe by DANTEC®.

and Lohse and Shishkina (2024), along with references therein. A more detailed analyses of statistical properties of the temperature field in RBC has been explored in recent experimental (He et al., 2018; Wang et al., 2019, 2022), theoretical (Shishkina et al., 2017; Olsthoorn, 2023), and numerical (Xu et al., 2021b) studies where the authors characterized boundary layer and mixing zone of convective flows. Some investigations aimed at describing buoyant thermal plumes departing from the thermal boundary layer, contributing to the overall heat flux through LSC in a wide range of Rayleigh numbers (Ra ranging from 10^7 to 10^{14}) (Liu and Ecke, 2011; van der Poel et al., 2015; Zhu et al., 2018; Blass et al., 2021; Reiter et al., 2021; Vishnu et al., 2022; Wang et al., 2022). Large-scale convective structures have been further explored through DNS, revealing relatively fewer plumes near the sidewalls carrying large heat fluxes, contrasted with more numerous plumes near the cell axis but with weaker heat fluxes, highlighting strong intermittency in this region (Lakkaraju et al., 2012; Chillà and Schumacher, 2012; Stevens et al., 2018; Pandey et al., 2018; Krug et al., 2020; Moller et al., 2021). The simulations also demonstrated the persistence of discrete thermal structures in RBC (Sakievich et al., 2016).

The studies also examined the effects of cell dimensions, revealing the variable nature of the LSC depending on the cell's aspect ratio ($\Gamma = \text{width}/\text{height}$) (Shishkina, 2021). The aspect ratio characterizing the facility (width = 2 m, height = 1 m, $\Gamma = 2$) corresponds to a single roll with a fixed orientation and pronounced oscillations about the mean position, a result of asymmetries inside the chamber (Anderson et al., 2021) (see Fig. 2). In cases where $\Gamma \gtrsim 4$, a three-dimensional, multi-roll structure has been observed (Bailon-Cuba et al., 2010; Ahlers et al., 2022). Large-scale convective structures have been further explored through DNS, revealing relatively fewer plumes near the sidewalls carrying large heat fluxes, contrasted with more numerous plumes near the cell axis but with weaker heat fluxes, highlighting strong intermittency in this region (Lakkaraju et al., 2012; Chillà and Schumacher, 2012; Stevens et al., 2018; Pandey et al., 2018; Krug et al., 2020; Moller et al., 2021). The simulations also demonstrated the persistence of discrete thermal structures in RBC (Sakievich et al., 2016).

It was recently showed that different regions of RBC can exhibit distinct local dynamics (He and Xia, 2019). As a result, applying a single physical mechanism to the entire convection cell may oversimplify the complex dynamics, as multiple types of force balance can coexist within the same system. On the other hand, studies on the Another aspect is the stability of the LSC have proved random reorientations and reversals as numerous analysis have proved its random reorientation and reversal in both cylindrical setups (Mishra et al., 2011; Wei, 2021; Xu et al., 2021a) (Brown and Ahlers, 2007; Mishra et al., 2011; Wei, 2021; Xu et al., 2016; Foroozani et al., 2017; Wang et al., 2018; Vishnu et al., 2020), without clearly indicating a superior choice.

The validity of Taylor's

Natural convection plays a crucial role in heat and mass transfer within the atmosphere. Despite its fundamental importance, several aspects of this phenomenon remain poorly understood even on a simplified level of controlled RBC conditions and require further investigation. One such example is the scaling of scalar fields, recently discussed by Kumar and Verma (2018). The authors examined the validity of the Taylor frozen hypothesis in the context of thermally driven turbulence of RBC, a widely used assumption in the atmospheric community, was examined in numerical simulations by Kumar and Verma (2018). The authors argued in RBC systems, concluding that the hypothesis holds true only when a steady LSC is present in the flow. They also cast doubt on the usability raised doubts about the suitability of the temperature field for determining whether the Bolgiano-Obukhov (BO, $-7/5$) or Obukhov-Corrsin (OC, $-5/3$) scaling is applicable for applies to turbulent convection. This uncertainty stems from the unclear power-law nature of temperature field ambiguous power law behavior of temperature spectra and the challenge of contrasting both challenges in comparing the associated scaling factors. Natural convection plays a crucial role in heat and mass transfer in the atmosphere. Despite its fundamental importance, certain characteristics of this phenomenon remain poorly understood and warrant further investigation. Similar concerns are highlighted in Lohse and Xia (2010), where the authors reviewed structure functions in RBC and suggested that the limited scale separation between the Bolgiano and outer length scales could be the main problem in obtaining BO scaling. In RBC systems, temperature serves as the primary driver of the convective mechanism rather than behaving as a passive scalar, leading to temperature spectra that may deviate from predictions based on passive scalar theories which are often applied in atmospheric analyses. Additionally, (He and Xia, 2019) demonstrated that a single RBC system can exhibit distinct local dynamics due to the coexistence of different types of force balances. Consequently, applying a single physical mechanism to describe the entire convection cell may oversimplify its complex dynamics.

From a microphysical perspective, which is the primary application of the chamber, understanding the spatial variability of scalar fluctuations within the chamber, including the properties of the LSC, is crucial. This understanding impacts not only the positioning of instruments inside the chamber but also the strategies for measurements, such as the lengths of measurement time series. Only with a comprehensive understanding of insight into the physics involved can different phenomena be effectively linked together. This is why analyses aimed at addressing the full spectrum of scales are the focus of the present study.

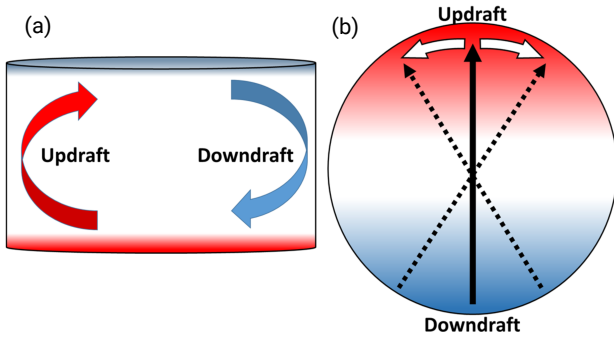


Figure 2. Schematic of the ~~cross-section of the~~ II Chamber **(a)** and its plan view **(b)** with the marked LSC. **(a)** The arrows represent the mean direction of the warm updraft (red) and the cool downdraft (blue). **(b)**. The dotted and white arrows show the azimuthal oscillations in the circulation. Figure from Anderson et al. (2021).

2 Methods

110 2.1 Setup and experimental strategy

In our measurements, we utilized the most recent version of the UFT, namely UFT-2B, as outlined in Section 1. The schematic representation of the complete UFT setup can be observed in Fig. 3. The sensor head was affixed to a 1 m probe support and linked to a specially designed 1 mA bridge/amplifier (AMP) using an approximately 1 m standard BNC cable. This amplifier was powered by four AA batteries. Subsequently, the analog signal was acquired by a 16-bit resolution digital-to-analog converter (DAC) from Measurement Computing Corporation (MCC). The DAC had a sampling rate of up to 100 kS s^{-1} (S stands for samples) and utilized the dedicated MCC software DAQami. Despite the time constant allowing for about 10 kHz data collection, we opted for an oversampling rate of 20 kHz to facilitate post-processing and filter out artifacts from other lab systems. Using two head sensors during this study, each possessing an approximate resistance of 30Ω , we attained a UFT sensitivity of approximately 75 mV K^{-1} after calibrating with a standard thermocouple.

120 For vertical profiling, the UFT was attached to a 6 mm diameter, 1.5 m long rod with a 90 degree bend at the end. The rod was marked in 3 cm increments to facilitate easy UFT positioning. A sturdy metal stand with two adjustable clamps was used to secure the rod in a stable, vertical position while allowing for the user to manually move the UFT to the desired location (see Fig. 3). To minimize potential movements of the UFT cabling and sensor head, both were affixed to the rod using simple adhesive, maintaining the wire in an upward and parallel orientation to the floor.

125 We studied the small-scale temperature structure within the convection environment across three temperature differences between the chamber's floor and ceiling: 10 K, 15 K, and 20 K, as detailed in Table 1. The setup included a cylinder, which is not shown in Fig. 3. For a more detailed schematic, please refer to Chang et al. (2016). The Rayleigh number was on the order of $\sim 10^9$ for the set boundary conditions and the chamber height of 1 m. We performed our calculations based on the formula suggested by Niedermeier et al. (2018), assuming dry convection with an estimated Prandtl number of 0.72.

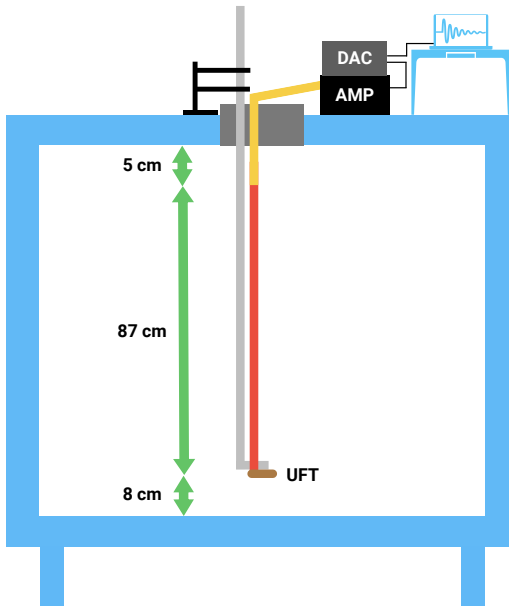


Figure 3. Schematic of the setup used during the measurements (diagram not to scale). At the top there was an operations center housing with most of the devices and cabling, including a BNC cable (yellow), an UFT amplifier (AMP), digital-to-analog converter (DAC), and a PC with a DAC software. Inside the II Chamber, a vertical rod with a curved end (gray) and a UFT sensor (brown) with DANTEC® probe support (red) attached to that end was deployed. The profiling limits were about 8 cm above the bottom and around 5 cm below the top layer. Note that, for clarity, the schematic does not include the cylinder.

130 Our primary focus was on examining the nature of scalar fluctuations throughout the entire vertical dimension, with a particular emphasis on regions near the floor and the ceiling. Consequently To achieve this, the UFT deployments featured irregular measurement positions (see Table 1) increasing slightly the spatial resolution of measurements near the both plates. Another consideration was the variable measurement time t , ranging from 3 minutes min to 19 minutes. This variability stemmed from the LSC period, $\tau_{12} \approx 72$ seconds (Anderson et al., 2021), and the uncertainty surrounding whether different 135 turbulence properties might be observed for shorter time segments min. To quantify whether the measurements are converged, we employed the framework provided by Lenschow et al. (1994). According to the results presented by the authors, when the ratio of the measurement time t to the large eddy correlation time T ratio gives $t/T \approx 10$, the data is within approximately 10% of the *true* value. Considering the turbulent properties, we link T with the large eddy correlation time for the turbulence 140 flow, which is estimated to be on the order of several seconds, 10 s in calculations, assuming a mean flow velocity of tens of centimeters per second. In this case, the averaging time of 3 min corresponds to approximately $18T$, whereas for 19 min time series it gives $114T$ indicating good convergence.

A less emphasized aspect was the surface topography. One configuration involved the presence of rough boundaries, consisting of aluminum bars (4 cm wide and 1.4 cm high) positioned on the floor and ceiling forming longitudinal stripes separated

by 17 cm intervals. The bars themselves were at a slightly different temperature compared to the rest of both panels (approximately 0.4 K). Subsequent UFT deployments were conducted after removing the bars, aiming to compare temperature fluctuation properties between the two cases. Unfortunately, a portion of the dataset is invalid due to high battery drainage, resulting in coverage of only one rough boundary case in this study.

As the surfaces inside the chamber reached steady temperatures (refer to Tab. 1), the UFT sensor was initially positioned 8 cm above the floor, near the axis of the cell. Due to the rod's length inside the chamber corresponding to its height, we had to wait for some time to allow the vibrations of the head sensor to dampen. This was really important after each position (h) change but played a crucial role especially in profiling the lower half of the measurement volume. The chamber's flange was covered with a thick foam layer, effectively reducing most mixing events near the opening. Although not an ideal solution, it seemed the most reasonable choice considering the ease of checking the UFT position, as well as the insulating and damping properties of the foam (when coating the rod).

Table 1. List of experiments together with the corresponding Π Chamber and UFT settings, and the Rayleigh numbers. Symbols explanation: T_F , T_C , T_W represent floor, ceiling, and walls temperature respectively, t stands for the measurement time at a given height h above the floor. Names of the experiments are made as follows: type of the measurement ("V" for vertical), ΔT , type of boundaries (S for smooth or R for rough), and time spent at a single position (L for 19 min or no marking for 3 min).

Experiment	rough/smooth boundaries	T_F [°C / K]	T_C [°C / K]	T_W [°C / K]	h [cm]	t [min]	$\text{Ra} [\times 10^9]$
V10-S-L	smooth	25 / 298	15 / 288	20 / 293	irregular	19	1.1
V10-S	smooth	25 / 298	15 / 288	20 / 293	8–95	3	1.1
V15-S-L	smooth	27.5 / 300.5	12.5 / 285.5	20 / 293	irregular	19	1.6
V15-S	smooth	27.5 / 300.5	12.5 / 285.5	20 / 293	8–95	3	1.6
V20-S-L	smooth	30 / 303	10 / 283	20 / 293	irregular	19	2.1
V20-S	smooth	30 / 303	10 / 283	20 / 293	8–95	3	2.1
V20-R	rough	30 / 303	10 / 283	20 / 293	8–95	3	2.1

The irregular positions are: 8, 14, 26, 35, 50, 65, 74, 86, 95 [cm].

After completing the measurements, the dataset underwent several basic preparations. These included the removal of electronic artifacts, signal despiking, Butterworth filtering (10th order, 2 kHz cutoff frequency), 2 kHz averaging, and the translation of values from voltage to temperature units. Additionally, each time series was consequently normalized by subtracting mean temperature value in the given position (see e.g., Fig. 4).

2.2 DNS methodology

Cloud Model 1 (CM1) (Bryan and Fritsch, 2002) in DNS configuration is used for these simulations. The model and setup are described in detail in Chandrakar et al. (2022, 2023). The computational domain size for DNS is $960 \times 960 \times 500$ grid

165 cells with a homogeneously 2.083 mm grid spacing in horizontal and stretched grid in vertical (finer near the top and bottom boundaries). CM1 solves the conservation equation set with the Boussinesq approximation and a prognostic pressure equation using a three-step Runge–Kutta time integration method with a fifth-order advection scheme. The Klemp–Wilhelmson time-
170 split steps are used for the acoustic terms in the compressible solver. The time integration of the governing equations uses an adaptive time step with a maximum Courant–Friedrichs–Lowy (CFL) number of 0.8. A no-slip boundary condition for all walls is applied, and the temperature boundary conditions (constant temperatures) are the same as the experimental setup. The simulations use molecular viscosity and thermal diffusivity values at the mean temperature (Prandtl number = 0.72). DNS is performed for the three experimental cases, V20-S, V15-S, and V10-S, listed in Tab. 1. Outputs from a steady-state period after the initial spin-up are used for the analysis. Consistent with the experiments, the Eulerian temperature time series are outputted at 0.0012–0.0015 s intervals from a region near the center of the domain (95–105 cm from sidewalls) at multiple heights from the bottom surface.

3 Results

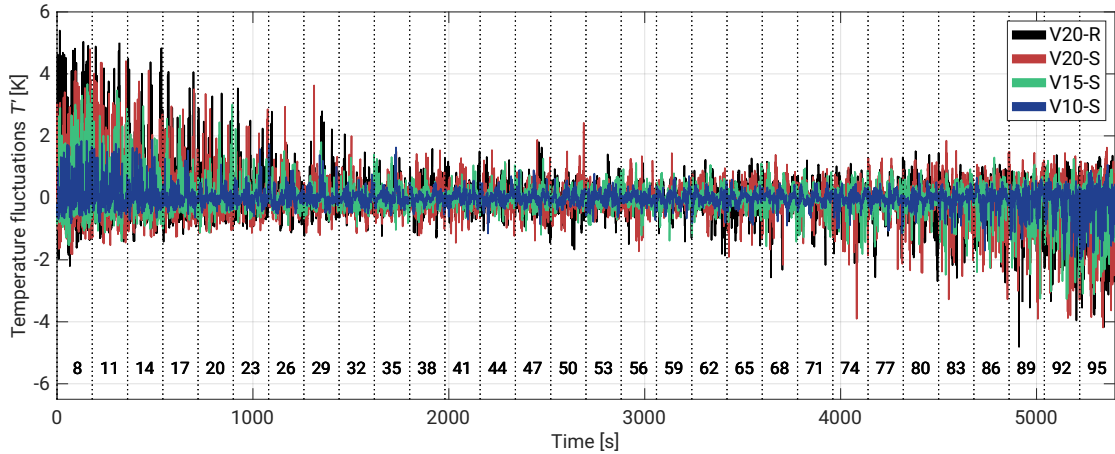
3.1 ~~Determination~~ Determination of basic characteristics of temperature profile

175 The top panel of Fig. 4 provides a sample of temperature fluctuations T' ($T' = T_h - \bar{T}_h$, where T_h represents the temperature series at a given height h , and overline denotes the mean) from the vertical scan of the measurement volume near the axis of the chamber. The skewed fluctuations observed in the closest proximity to the plates serve as expected temperature evidence of ~~RBC in the cell~~ thermal plumes characteristic for RBC. We can observe a smooth transition involving gradual suppression of fluctuations or rather gradual decrease in occurring thermal plumes as the sensor moved towards the mid-height plane. The
180 reverse symmetry is present in the upper half of the cell. The nature of these fluctuations aligns with the numerical results of heat fluxes in the bulk region obtained by Lakkaraju et al. (2012), temperature time series reported in He and Xia (2019) and Wang et al. (2022), and experimental data provided by Anderson et al. (2021). However, it is noteworthy that all these works primarily focused on specific regions of the cells, lacking a more detailed insight into the temperature characteristics, especially considering the limited temporal resolution of the used instrumentation.

185 The most substantial temperature fluctuations are observed near the floor region. In cases with a flat surface (experiments summary in Tab. 1), peaks oscillate around 4 K, while rough boundaries scan exhibit fluctuations exceeding 5 K. As the sensor approaches the mid-high plane, the differences between $\Delta T = 20$ K cases become negligible. Similarly, no distinctions are apparent near the upper plate, with a maximal amplitude at the level of –4 K for both V20-S and V20-R.

190 In the bottom panel of Fig. 4, two vertical layouts are presented, each illustrating 10 min series near both plates positions and segregating T' based on the given ΔT . The evident reverse symmetry is notable; however, it is important to highlight that there are varying amplitudes of fluctuations in each corresponding pair of graphs (same ΔT but distinct h). This variation may result from weaker thermal plumes departing from the top plate, as well as from the not perfectly insulated chamber's flange (mentioned in 2.1), which could lead to minor mixing in the vicinity of the sensor deployment spot. For a more in-depth examination of the temperature fluctuations near both plates, refer to Appendix A.

(a)



(b)

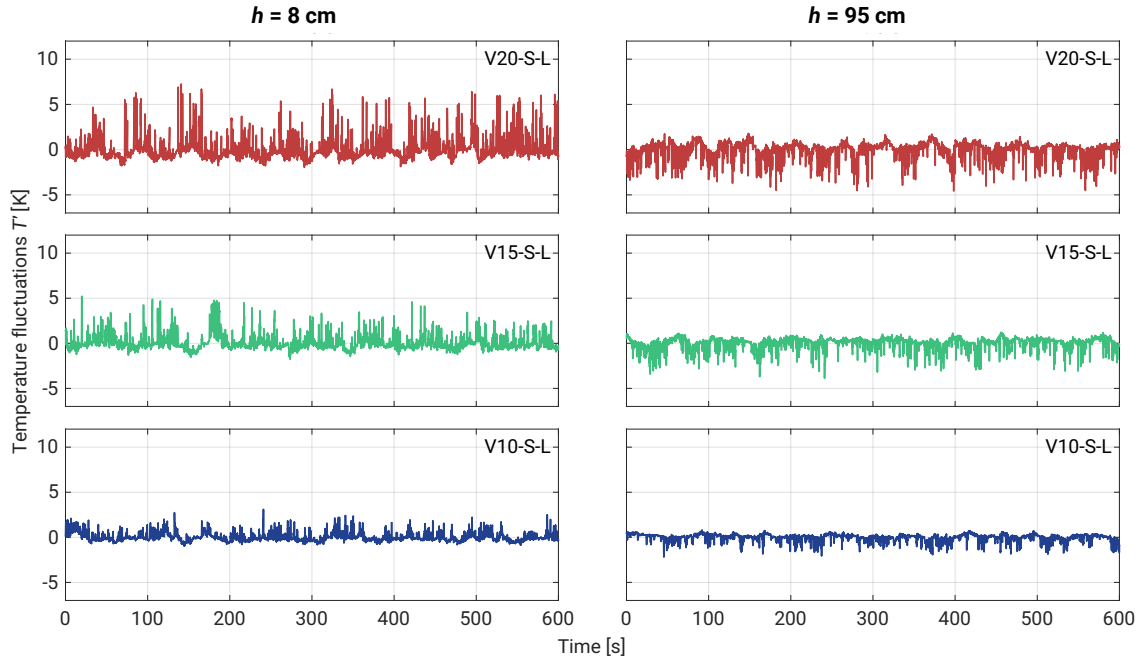


Figure 4. Temperature fluctuations T' time series corresponding to different ΔT that are described in Tab. 1. Top panel (a) corresponds to shows time series collected during full vertical scan scans with the consecutive changes of the sensor positions across the chamber. The horizontal row of numbers at the bottom denote the position of the UFT heights in centimeters with respect to above the lower plate. The chart includes 3 min series. Bottom layouts Lower panels (b) represents 10 min measurements near the floor ($h = 8$ cm), and just below the ceiling ($h = 95$ cm, 5 cm below the top plate).

195 The temperature fluctuations also manifest oscillations, particularly noticeable in the case of $\Delta T = 20$ K near the plates. However, these oscillations gradually diminish as the temperature difference decreases and as the sensor moves toward the center of the cell. Analyzing V20-S-L at both heights, the periodicity appears irregular but is of a same order of magnitude as observed by Anderson et al. (2021) and therefore corresponds to the LSC. Previous studies have highlighted that the LSC can exhibit various modes around its mean position, leading to phenomena such as out-of-phase oscillations at the top and bottom
200 of the chamber (torsional mode, see Funfschilling et al. (2008)), as well as side-to-side oscillations (sloshing mode, see Xi et al. (2009); Brown and Ahlers (2009)). Cells with very high symmetry might be also characterized by spontaneously cease and reorientation of the LSC to different angular position (Brown and Ahlers, 2009). All these effects are beyond the scope of this investigation but the raw measurements give clear evidence of changing temperature oscillations near both plates.

205 In Fig. 5, the standard deviation $\sigma_{T'}$ is presented in relation to the sensor position within the cell chamber and illustrates the dependence of the fluctuation level, corresponding to the top panel of Fig. 4. The highest $\sigma_{T'}$ values are observed near both plates, particularly with a clear dominance with the maximum at the bottom. This asymmetry diminishes as ΔT decreases, starting with an approximate 0.4 K disparity in V20-R and concluding with about a 0.1 K shift in V10-S-L. It's noteworthy that extended measurements yield slightly different values, reflecting a more robust convergence as opposed to 3 min cases. The bulk region exhibits relatively constant values with comparatively small deviations. Additionally, this region experiences
210 the smallest differences between corresponding ΔT values. Decreasing ΔT shifts left $\sigma_{T'}$ values and damps T' in the whole volume. In Fig. B1a we provide non-dimensionalized form of standard deviation.

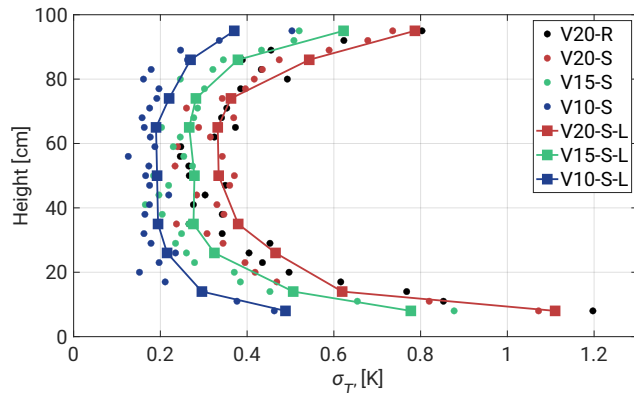


Figure 5. Standard deviation $\sigma_{T'}$ with respect to the height position of the chamber sensor. Short time series (3 min) are denoted by circles, squares represent longer measurements (19 min). Decreasing ΔT shifts left $\sigma_{T'}$ values reducing the temperature fluctuations at all positions.

215 The surface topography contributes to slightly higher $\sigma_{T'}$ values, primarily in the closest vicinity of the plates. This effect may be attributed to the elevated surface level, potentially leading to varied stages of thermal plume development at the same measurement position. However, these thermal structures are getting mixed with the surroundings, producing approximately equivalent results just a few centimeters higher. As previously mentioned, recent work by He and Xia (2019) emphasizes He and Xia (2019) emphasized that each region of the RBC can exhibit its local dynamics, a consequence of over-

lapping mechanisms that act as drivers for each other. In this specific case, the LSC induces ~~a~~ mixing of all thermal structures originating from the surface, ~~and it~~. It can also turbulently propel ~~the~~ thermal plumes due to ~~the~~ irregular topography. The resulting mixing and stronger turbulence in this region might be responsible for the thermal peaks observed in the top panel of 220 Fig. 4.

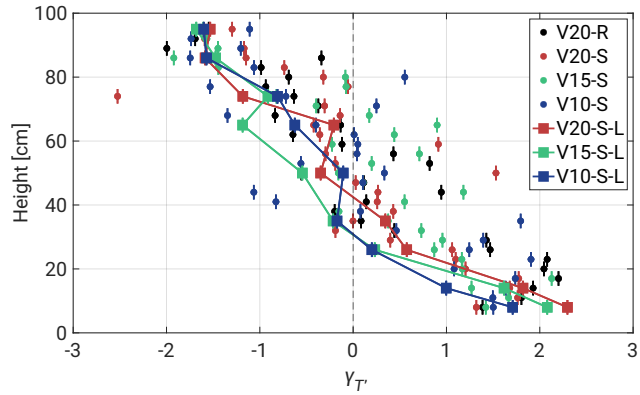


Figure 6. Skewness $\mu_{T'}$ with respect to the height position of the chamber sensor. Short time series (3 min) are denoted by circles, squares represent longer measurements (19 min). ~~Included uncertainties~~ Uncertainties were calculated using formula $\delta_{\mu_{T'}} = \sqrt{\frac{6N(N-1)}{(N-2)(N+1)(N+3)}}$ $\delta_{\mu_{T'}} = \sqrt{\frac{6N(N-1)}{(N-2)(N+1)(N+3)}}$ where N denotes the number of samples.

In Fig. 6, the skewness of T' , denoted as $\mu_{T'}$, is analyzed with respect to the vertical positions within the chamber. We use adjusted Fisher–Pearson standardized third moment, expressed as $\mu_{T'} = \frac{N^2}{(N-1)(N-2)} \frac{\bar{T}'^3}{\sigma_{T'}^3} \gamma_{T'} = \frac{N^2}{(N-1)(N-2)} \frac{\bar{T}'^3}{\sigma_{T'}^3}$, where N represents the number of samples. The findings confirm previous observations, showing positive skewness (associated with warm plumes) near the floor and negative skewness (indicative of cold plumes) just below the ceiling. The third moment is 225 notably influenced by rare events, leading to significant fluctuations in the 3 min dataset but mostly averaged out in longer segments, resulting in more consistent curves.

The regions near both plates demonstrate a high convergence of $\mu_{T'}$ values with minimal deviations. An interesting observation is noted at ~~the~~ a distance of 8 cm ~~region~~ above the floor, where the 3 min records initially exhibit a skewness of about 1.4. This area likely experiences a higher frequency of intense thermal plumes, resulting in a broader range of temperature 230 fluctuations (refer to Fig. 5). ~~It has been shown in previous studies that thermal plume detachment introduces large fluctuations in temperature and velocity boundary layer thickness and lead to further LSC interactions as distance from the plate grows (Wagner et al., 2012; Shi et al., 2012; De et al., 2018; Shevkar et al., 2022). Similar effects might be responsible for what we observe.~~ As the plume structures develop, $\mu_{T'}$ increases to approximately 2. Then, at the 20 cm level, there is a subtle 235 indication of ~~possible~~ change in the thermal dynamics of the system. This change may be associated with specific transitions in convective flow patterns and more intense interaction of thermal plumes with the LSC in the ring layer around the walls and plates (see Fig. 2a). Moving further away from the heated floor, the LSC ~~dominates~~ is likely dominating the existing structures,

increasing the dissipation of thermal energy and leading to a decrease in skewness. This results in thermal structures becoming more dispersed, leading to a narrower and less extreme distribution of temperature fluctuations.

However, not all thermal plumes ~~are could be~~ fully averaged out, especially as the flow around the cell decreases towards 240 more central regions. This ~~allows might allow~~ some remaining plume structures to reach the central region between 40–70 cm ~~, mixing and resulting and mix which could result~~ in positive skewness (bottom plumes carry higher energy). ~~This Similar~~ behavior might be also observed in longer records, manifesting as fluctuations in ~~#T-γT~~ within the 50–70 cm segment. Importantly, the positions of these shifts do not appear to be directly dependent on ΔT .

A comprehensive understanding of the thermal dynamics requires additional information on the small-scale temperature field 245 around the axis, its velocity field, and a detailed description of the LSC time evolution. ~~From the perspective of microphysical processes in future moist experiments, the Lagrangian histories of droplets or aerosols carried by thermal plumes—or alternatively located in the volumes between them—can theoretically lead to different droplet sizes (Chandrakar et al., 2018b, 2023). The local variability of $\sigma_{T'}$ and $\gamma_{T'}$ indicates that, over short timescales, droplets present in a given volume of the chamber may develop differing growth habits.~~

250 Upon comparing the topographic effect, we did not observe any major differences and concluded that 3 min records might be insufficient to investigate the impact caused by the presence of roughness. However, recent numerical work by Zhang et al. (2018) (for $10^7 \leq \text{Ra} \leq 10^{11}$ and fixed $\text{Pr} = 0.7$) indicates that there is a critical roughness height h_c below which the presence of roughness reduces heat transfer in RBC. The authors link this phenomenon with fluid being trapped and accumulated inside the cavity regions between the rough boundaries. Our approximate calculations for the II Chamber setup indicate the h_c of 255 approximately 7 mm, compared to the 1.4 cm height of the tiles.

3.2 Power Spectral Densities

Power Spectral Density (PSD) of T' was computed using the Welch algorithm. Initial analyses were primarily directed towards 260 estimating the LSC periods τ for the given ΔT and with respect to the measurement position (see Fig. 7a). This involved utilizing 19 min datasets with window lengths approximately equal to the size of the collected segments. Employing a 50% overlap between segments and incorporating a high number of discrete Fourier transforms (eight times the window length), we derived estimates of the LSC periods along with their associated standard deviations. For $\Delta T = 10$ K a modest convergence of data points is observed, particularly notable within the 60–80 cm region. This resulted in relatively elevated standard deviation (grey areas denote $\pm 1\sigma_\tau$), yielding a period of approximately $\tau_{10} \approx 79$ s. Subsequent ΔT demonstrated a more uniform distribution across all levels, accompanied by a gradual reduction in the LSC period to approximately $\tau_{15} \approx 65$ s and $\tau_{20} \approx 57$ s.

265 The relationship between τ and ΔT , modeled by ~~exponential the power law~~ function τ^e , is illustrated in Fig. 7b. The fit exhibits narrow 95% prediction bounds in the fitted region but significantly large bounds outside. The model was constructed using a sparse dataset consisting of only four data points, including the result obtained by Anderson et al. (2021) at $\Delta T = 12$ K. Consequently, this limited dataset may not fully capture the true relationship, particularly at lower ($\Delta T < 10$ K) and higher ($\Delta T > 20$ K) temperature differences. The potential discrepancies could be attributed to a stronger diffusion dominance over 270 convection at lower ΔT or more pronounced overlapping thermal plumes at higher temperatures, respectively.

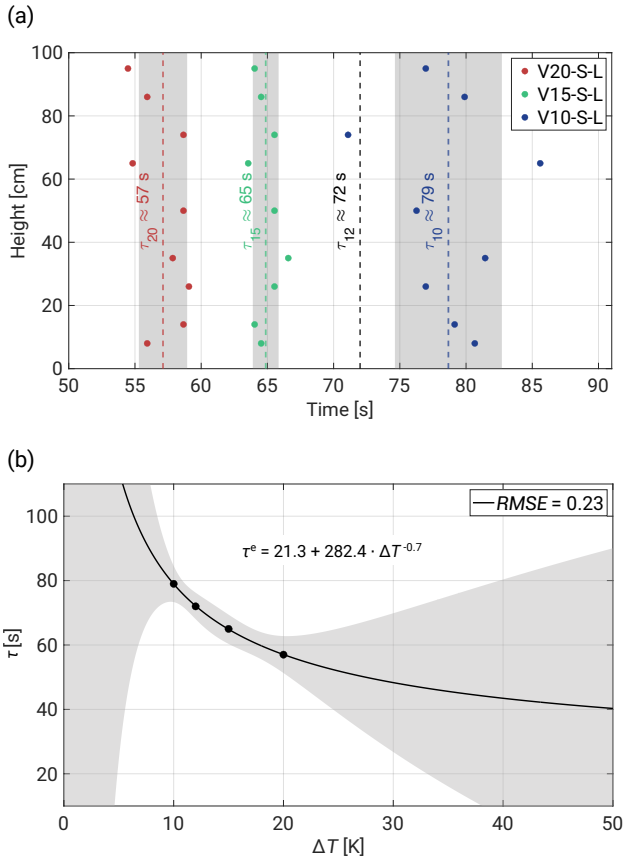


Figure 7. Vertical variability of the Measured LSC period periods with respect to ΔT and vertical position of the sensor. (a) Grey regions describe $\pm 1\sigma\tau$ and the black dashed line denotes the result obtained by Anderson et al. (2021) for $\Delta T = 12$ K. (b) The relationship between τ and ΔT modeled by exponential the power law (τ^e) function. The plot includes 95% simultaneous functional bounds, fitted equation, and root mean squared error ($RMSE$).

In subsequent PSD analyses, we continued using only 19 min records, as shorter measurements exhibit too much variability in spectra due to their duration being comparable with the LSC periods. This time-modified window length, approximately 1/9 of the total segment with windows overlapping by half of their length, resulted in 17 individual PSDs that were averaged. This approach enhances chart readability while maintaining fidelity to the spectral slopes. To collapse the curves representing 275 measurements from different positions, we followed the scaling method proposed by Zhou and Xia (2001). Fig. 8a plots the scaled $f^2 P(f)$ spectrum for the V20-S-L case, enabling determination of the peak frequency f_p , around which the PSDs become universal functions. In this case, f_p oscillates around $f = 4$ Hz, exhibiting high convergence across all curves.

In Fig. 8b, we provide a sample of scaled PSD $P(f)/P(f_p)$ versus f/f_p in the lower half of the chamber and define three spectrum regimes. Based on the scaling method proposed by Kumar and Verma (2018) and Zhou and Xia (2001), we conducted 280 also a similar analysis in the wavenumber domain. For more details, please refer to Appendix C. To estimate the slopes, we

employed a methodology outlined in Siebert et al. (2006) and Nowak et al. (2021), averaging raw spectra over equidistant logarithmic frequency bins (twenty bins per decade in our case) and ~~fitting using exponential functions. Additionally, to assess the linearity of the slopes in then fitting power law functions. To obtain the best possibly fit we selected spectra regions based on the highest log-log coordinates, we computed linearity criteria using~~ the Pearson correlation coefficient p for the resampled 285 points.

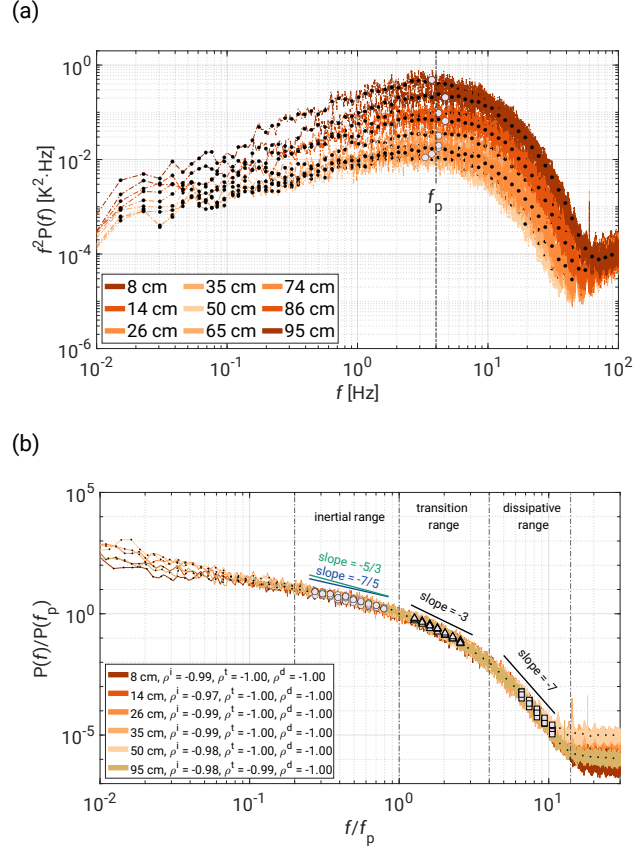


Figure 8. Scaled V20-S-L PSD with respect to the UFT positions (color gradients) in the lower half of the chamber (plus top position). **(a)** Scaled spectrum of $f^2 P(f)$ with marked mean f_p value, $f_p \approx 4$ Hz. **(b)** PSD $P(f)/P(f_p)$ versus $f/(f_p)$ with three defined regimes: inertial range (circles, $0.2 \leq f/f_p \leq 1$), transition range (triangles, $1 \leq f/f_p \leq 4$), and dissipative range (squares, $4 \leq f/f_p \leq 20$). Each regime is denoted by different markers with an approximate slope value added above curves. The Pearson correlation coefficients p have upper indices to indicate the regimes.

~~In-Extended discussions on passive scalar spectra scaling can be found in works such as Gotoh and Yeung (2012) and Sreenivasan (2019). We adapted the graph from the former study for Fig. 9, which illustrates possible spectral slopes as a function of the Pr number. For our experimental conditions, the results are expected to align with the scaling for $\text{Pr} \approx 1$. In~~

the following paragraphs, we aim to contextualize our findings within the broader scope of the literature and address potential explanations for observations that have not yet been described.

In Fig. 10a, the regime $0.2 \leq f/f_p \leq 1$, marked by circles, in the literature is referred to as the inertial-convective regime which is associated with OC scaling, where the temperature field (acting as a passive scalar) does not influence the flow dynamics (Castaing, 1990; Cioni et al., 1995; He et al., 2014). However, in thermally-driven convection flow is not passive but the flow is actively driven by temperature (buoyancy)–temperature-induced buoyancy differences. This regime is defined in the literature range is therefore redefined as the inertial-buoyancy range, with the scalar (temperature) spectrum following where the temperature spectrum follows BO scaling (Chillá et al., 1993; Ashkenazi and Steinberg, 1999; Zhou and Xia, 2001). Conversely, OC scaling is reported in the inertial-convective range, where temperature (scalar) is assumed to be passive and has no influence on the flow dynamics (Castaing, 1990; Cioni et al., 1995; He et al., 2014). Our analysis provides no definitive answer, as the slopes oscillate between OC and BO scaling, with a slight bias toward $-7/5$. However, as previously noted, the two slopes are too close to be easily distinguished (see Fig. 8b). Thus, we classify this range simply as the inertial range without committing to a specific scaling profile. Interestingly, Niemela et al. (2000) ($10^6 \leq Ra \leq 10^7$) and Pawar and Arakeri (2016) (axially homogeneous buoyancy-driven turbulent flow, $10^4 \leq Ra \leq 10^9$) observed both scaling behaviors in their experiments. In the latter study, the authors debated whether the results indicated The latter study raised the question of whether these results indicate dual scaling or a gradual steepening of the spectrum.

In our case, the regime of $0.2 \leq f/f_p \leq 1$, indicated by circles in Fig. 10a, exhibits relatively small variability of PSD slopes. This range was selected based on the highest Pearson correlation coefficient, which limited the fitting region. Our analysis provides no clear answer, as the slopes oscillate between OC and BO scaling, with a slight bias towards $-7/5$. However, as mentioned earlier, the two slopes are too close to each other to be easily distinguished (see Fig. 8b), leading us to label this regime as the inertial range without its specific profiling.

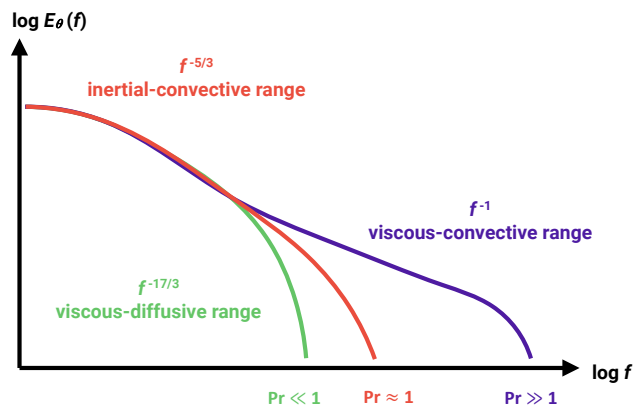


Figure 9. Schematic of passive scalar spectrum depending of Pr regime. Figure based on the graph from Gotoh and Yeung (2012) with minor modifications.

310 The No direct references in the literature address the subsequent regime scalings (~ -3 and ~ -7) or the roll-off region of the scalar spectrum (see Fig. 9). Recent investigations of the dissipation range in the energy spectrum only began exploring this regime suggesting a superposition of two exponential forms (Khurshid et al., 2018; Buaria and Sreenivasan, 2020). Therefore, our further discussion will explore potential connections between our and other results in convective flow research.

315 RBC dynamics span a wide range of scales, including thermal plumes, vortices, and the LSC, with complex interactions between these structures (Fernando and Smith IV, 2001; Xi et al., 2004; Zhou et al., 2016; Guo et al., 2017; Chen et al., 2018; Pandey et al.). These overlapping processes likely influence the observed spectra. Recent LES studies on thermal plumes have revealed additional insights into scalar spectral scaling (Chen and Bhaganagar, 2021, 2023, 2024). Using a heated surface experiment, the authors reported density and temperature spectra scaling as -2.7 , strongly correlated with the velocity spectrum. Furthermore, vertical heat and mass fluxes exhibited a -3 scaling, matching the vertical component of the turbulent kinetic energy (TKE) 320 spectrum. This corresponds with the regime $1 \leq f/f_p \leq 4$, indicated marked by triangles in Fig. 10a, which is characterized by slopes oscillating around -3 , with slightly higher variability greater variability observed for the V10-S-L case.

~~There is no direct reference in the literature for such slopes, and further considerations should explore possible connections between our findings and known explanations.~~

325 The first set of explanations follows the rich dynamics of RBC and studies on two- and three-dimensional turbulence. Foundational works in this field include Batchelor (1959) and Kraichnan (1967, 1968), which introduced a specific regime of scales called the viscous-conveective range. In this regime, scalar fluctuations are influenced by both turbulent flow and viscous dissipation, but molecular diffusion remains relatively small. In 1967, Kraichnan explored the Batchelor regime in ~~Moreover, in the papers by Chen and Bhaganagar both spectra of 2D~~, providing a dual cascade model of inverse energy transfer and direct enstrophy cascade associated with interactions of vortices and larger coherent structures. The given energy scaling 330 spectra were $-5/3$ and -3 , respectively. The latter corresponds with the mentioned viscous-conveective range, which, in the case of the scalar variance spectrum, should follow -1 . As described in the overview paper by Alexakis and Biferale (2018), the coexistence of cascades at the same scales is possible, making the outcome spectrum a result of either cascading process. It is also possible for the spectrum to be a TKE, horizontal structures of 3D TKE, as well as helicity, consistently exhibited 335 slopes of $-5/3$ and -3 , respectively with the observed regime change found around wavenumber $k = 10$ which is consisted with our results showed in Appendix C. Their flux analysis revealed inverse TKE and helicity cascades toward large structures and forward cascades of these invariants for the small scales. Further studies on velocity-based longitudinal structure functions (2nd, 3rd, and 4th moments) showed that the scaling exponents fell between theoretical predictions for 2D and 3D systems. For example, strong vertical confinement or anisotropic Fourier mode distributions can mimic 2D dynamics in certain ranges (Musacchio and Boffetta, 2019; de Wit et al., 2022; Alexakis, 2023). Consequently, energy cascades and their directions are 340 highly scale-dependent, influenced by invariants such as enstrophy and helicity, potentially resulting in the coexistence of multiple cascades and the superposition of power laws, with each cascade determining the energy spectrum at different ranges of scales. The authors clearly note that the presence of multiple cascades at the same scales does not imply that both invariants cascade in the same direction. Earlier research by Cencini et al. (2011) showed an intriguing result of the coexistence of both forward and reverse cascades in a situation where energy injection takes place at multiple scales in law spectra. Detailed

345 discussions on cascades and transitions in turbulence are provided by Alexakis and Biferale (2018). However, in the II Chamber we do not recognize strong anisotropy and only regions near the top and bottom plates could potentially exhibit such quasi 2D turbulence.

350 Based on numerous studies over the years, it is evident that RBC effects whereas similar spectra slopes are observed in the whole volume of the chamber. On the other hand, in 3D exhibits very complex dynamics in a wide range of scales, including thermal plumes, vortices, and LSC with their mutual interactions (Fernando and Smith IV, 2001; Xi et al., 2004; Zhou et al., 2016; Guo et al., 2018), making it possible for the spectra to be a result of these overlapping processes. Moreover, it seems legitimate to ask to what extent theories based on strong assumptions like turbulence, large-scale stirring can introduce helicity, modifying cascade directions and contributing sub-leading corrections depending on the helicity's sign (Eidelman et al., 2014; Yan et al., 2020; Plunian et al., 2022). The exact role of helicity in energy transfer mechanisms remains unclear and is an active area of research (Yao and Hussain, 2022)

355 ~

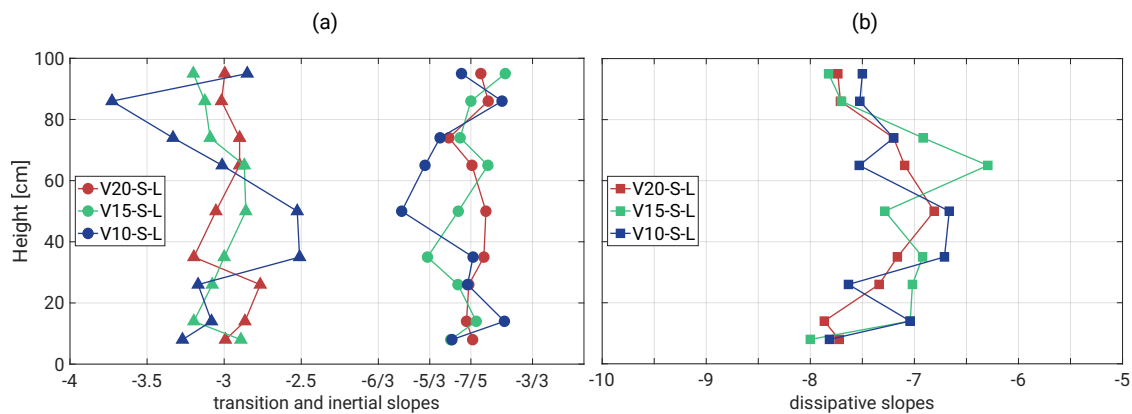


Figure 10. Panel of fitted slopes. (a) corresponds to transition and inertial ranges respectively whereas (b) describes dissipative regime.

Given this complexity, it is reasonable to question whether theoretical assumptions such as isotropy, homogeneity, stationarity, and self-similarity might be sufficient to fully uncover the physical reality, emphasizing the role of anisotropy are sufficient to capture the full physical reality. Anisotropy and non-stationary coherent structures. The real flow might deviate from theoretically predicted spectra scaling, requiring more complex characterization likely play significant roles, potentially causing deviations from predicted spectral scaling. In the given full spectrum analysis, the nature of the scale break we observe around $f/f_p \approx 1$ might be linked, e.g., to the dynamic transition between LSC scale dominance, where larger coherent structures form, and the regime of smaller-scale thermal plumes and vortices, which might eventually lead to overlapping power laws and ultimately modifying the final spectra. As an example we present in the Appendix D, an additional analysis showing an estimation of the thermal plumes dominance region close to the chamber center. Based on He and Xia (2019), the logarithmic dependence of σ_T on chamber height is demonstrated, which can be interpreted as the balance of buoyancy and inertial forces.

370 The second group of possible explanations for the -3 scaling regime emphasizes that buoyancy effects in RBC are due to temperature forcing, which RBC, temperature forcing drives both large- and small-scale structures. Already mentioned overview by Alexakis and Biferale (2018) points out that making, complicating the universality of passive and active scalar theories. Alexakis and Biferale (2018) emphasize that strong assumptions about cascades, including their directions, is and their directions are not feasible for active scalars. Further arguments highlight the lack of universality between passive and active quantities, particularly in scenarios where there is a strong relationship between, particularly when velocity and scalar fields are strongly coupled. This leaves open questions about preferential sampling effects of forcing along Lagrangian trajectories of the active scalar field.

375 The complexity of mentioned problems extends beyond the scope of this paper. In the given full spectrum analysis, the nature of the spectral break observed near $f/f_p \approx 1$ may be linked to a transition between LSC-dominated scales, characterized by large coherent structures, and smaller-scale thermal plumes and vortices. These overlapping power laws could ultimately shape the observed spectra. Consequently, we classify interpret the -3 regime as a transition range between buoyancy-scale processes and molecular dissipative scales. Additional analysis presented in Appendix D estimates the dominance of thermal 380 plumes near the chamber center. Following He and Xia (2019), we demonstrate a logarithmic dependence of σ_T on chamber height, reflecting a balance between buoyancy and inertial forces.

385 Based on Finally, our high-frequency measurements, we estimated slopes in indicate that the dissipative regime to be around slopes are approximately -7 (see Fig. 10b). Slope The slope distribution with respect to chamber height is symmetrical, with the highest reaching the steepest values near the plates ($\approx -8 \sim -8$) and the smallest in the bulk region (≈ -7). There are no direct references in the literature justifying similar slope values. However, similar spectral characteristics can be found in the figures (≈ -7). According to Sreenivasan (2019), no scalar spectrum description exists for the dissipative regime. While the energy spectrum in this range can be represented by an exponential form, our findings suggest that for the scalar field, even a single power law is sufficient. Corresponding characteristics are visible in Niemela et al. (2000) and Zhou and Xia (2001), though without extensive discussion on slopes. There is also a potential connection with the spectral scaling of $-17/3$ in 390 the so-called inertial-diffusive range as proposed in Kraichnan (1968). This continues previous considerations on the complex dynamics in RBC and the nontrivial sealings observed in many experiments although these studies provide limited discussion on the observed slopes.

395 Panel of fitted slopes. (a) corresponds to transition and inertial ranges respectively whereas (b) describes dissipative regime. Worth noting is also the variability of the noise level (starting around $f/f_p \approx 12$) with respect to the chamber height, with its highest values linked to the bulk region and the lowest (10 times magnitude difference) representing regions near the plates (see Fig. C1 in Appendix C). This phenomenon is attributed to the mean velocity field and its strong reduction in the central areas of the cell causing the noise to rise.

3.3 DNS versus experimental data

400 Another goal of the presented study was to compare the experimental results obtained with the UFT and the corresponding DNS data. The essential details on the DNS methodology and properties of the series can be found in Sec. 2.2. Our approach

was to repeat the analysis and to retrieve both basic characteristics of temperature profile and information on PSD at different cell's levels. Sample series can be seen in Fig. A1 and Fig. A2.

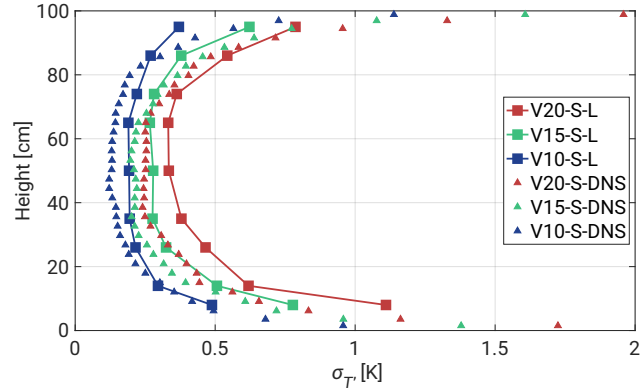


Figure 11. Standard deviation $\sigma_{T'}$ with respect to the height of the chamber. The chart analogical to Fig. 5 but including only 19 min segments (squares) and the DNS (triangles).

As presented in the Fig. 5 standard deviation distribution in the chamber is almost symmetrical with respect to the center with a small bias near the ceiling. The difference is attributed to the not perfectly insulated flange during UFT position adjustments. 405 Fig. 11 present analogous study but with the DNS data covering exactly same thermodynamic conditions in the cell. Since the vertical grid size spans from about 1 mm near the plates to about 2.3 mm at the center, the available range significantly improves comprehensiveness of boundary layers. The limit regions exhibit maximum deviation of $\sigma_{T'} \approx 2$ K with a tiny bias in the vicinity of the upper plate. Also the shape of the curves is more bumped up in the center and slightly shifted left what might 410 be an analogy to 3 min records in the Fig. 5. The numerical data provide more stable monotonicity but represents equivalent periods of time. In Fig. B1b there is non-dimensionalized form of this figure.

Similar conclusions can be made in terms of skewness profiles in Fig 12a. The DNS data exhibits much smaller fluctuations than corresponding 3 min UFT segments but preserve the general tendency near the floor and in the central region. The characteristic jump in ~~HTT-XL~~ is observed not around 20 cm but in half way. On the other side, a symmetrical jump is also observed near the ceiling what was not revealed in the UFT measurements likely due to a very shallow layer of thermal 415 plume regime (the UFT measurements ended about 5 cm below the ceiling). Also the mixing region between 40–70 cm is reestablished resulting in higher deviations for lower ΔT . The skewness distribution contributes to the mean vertical profile in the cell (see Fig. 12b). The presence of both positive (~ 40 cm) and negative (~ 80 cm) velocity jumps drives dynamics in the bulk region, facilitating the mixing of cold and warm plumes. The horizontal components of the flow follow the LSC directions giving mean values of 15 cm/s near the plates. A more comprehensive discussion on the dynamics of the thermal plumes can 420 be found in Sec. 3.1.

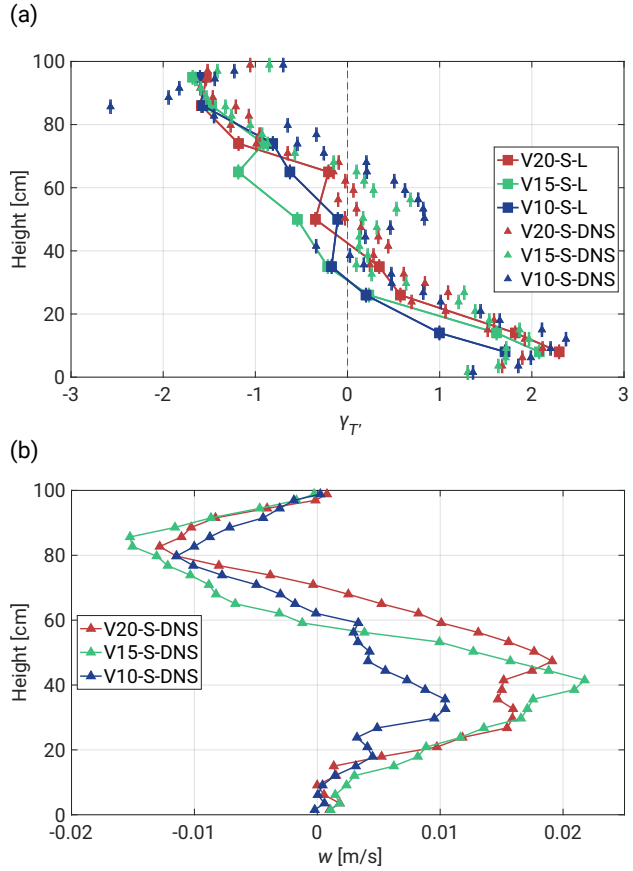


Figure 12. (a) Skewness μ_T' with respect to the height γ_T' , as a function of height within the chamber supported by the 3 min DNS data. The chart analogical to Fig. 6 but including only 19 min segments (squares) and the DNS numerical time series (triangles). (b) Mean vertical flow profile provided by the DNS.

4 Summary

Our objective was to enhance understanding of thermally-driven convection in terms of small-scale variations in the temperature scalar field. We conducted a small-scale study on the temperature structure of RBC in the II Chamber using three different temperature differences (10 K, 15 K, and 20 K) at Ra of approximately 10^9 and Pr of 0.7. Measurements were carried out

425 The objective was to improve our understanding of thermally-driven convection by analyzing small-scale variations along the chamber's axis. Measurements were performed using a miniaturized UltraFast Thermometer operating at 2 kHz, allowing enabling undisturbed vertical temperature profiling from 8 cm above the floor to 5 cm below the ceiling. Unlike classical RBC studies, this research is characterized by relatively short measurement durations of 19 min and 3 min, which fall below the typical record lengths for such experiments. Nevertheless, the primary goal was to link this work with other experiments 430 conducted in the II Chamber. Its main objective is to investigate microphysical processes relevant to the real atmosphere, such

as supersaturation fluctuations crucial for cloud formation and development. Small-scale temperature profiling under varying conditions, as typically observed in the chamber, provides valuable insights that could inform future experiments and address related scientific questions. The key findings of this study are summarized below.

435 – **basic characteristics****Basic Characteristics:** We observed significant changes in the standard deviation and skewness of the distribution of temperature fluctuations near the top and bottom surfaces. Additionally, we see variations in the **sealing exponents of the power spectrum spectra scaling** in these near-surface regions. The turbulence in the center of the chamber exhibited characteristics more akin to homogeneous, isotropic turbulence. These observed variations were attributed to the dynamics of local thermal plumes and their interaction with the large-scale circulation (LSC). Both 19 min and 3 min measurements were consistent, although the shorter records showed higher variability in standard deviation and skewness distribution. The statistical properties of the temperature field obtained in **RBC** the **II Chamber** may offer insights into thermal **processes structures development** in the atmospheric surface layer, thereby enhancing our understanding of **its thermal structure surface-air temperature fluctuations characteristics with respect to the thermal conditions** (Kukharets and Nalbandyan, 2006). Furthermore, the analysis of large-scale coherent structures in RBC provides a framework for **understanding broader perspective on** thermal circulations, as well as the distribution of temperature and moisture, both in cloud chambers (Anderson et al., 2021) and by analogy in the lower atmosphere (Zhou and Xia, 2013; Moller et al., 2021). The chamber is not designed for idealized RBC experiments. Its structure solutions (e.g. windows on sides, atypical side-wall boundary conditions) aimed at cloud microphysics research is revealed in asymmetries of the profiles of temperature fluctuations statistics.

440 445 – **topographic effects****Topographic Effects:** No major differences were observed corresponding to topographic effects, likely due to insufficient time series. However, numerical work by Zhang et al. (2018) shed light on the necessary roughness height for robust heat transfer in RBC. Below the critical point, the authors observed trapped and accumulated heat inside the cavity regions between the rough boundaries.

450 455 – **dynamic regimes****Dynamic Regimes:** PSD analysis revealed periodicity of LSC with respect to the temperature differences, characterized by **an exponential the power law** formula consistent with previous findings (Anderson et al., 2021). We identified three distinct dynamic regimes: an inertial range (with slopes **around of** $\sim -7/5$), a transition range (slopes **around of** ~ -3), and a dissipative range (slopes **around of** ~ -7). The scale break between the inertial and transition ranges was attributed to a dynamic transition from the LSC-dominated regime to the thermal plume regime. Appendix D demonstrated that this transition is also observable in the spatial domain. Our findings are consistent with other studies not directly related to RBC though. For example, a similar scale break between inertial and transition ranges was observed in temperature fluctuation measurements near the surface of Jezero Crater on Mars (de la Torre Juárez et al., 2023), whereas **corresponding** slopes of $-17/3$ **and** -3 have been reported in power spectra of solar surface intensity variance field, attributed to buoyancy-driven turbulent dynamics in a strongly thermally diffusive regime (Rieutord et al., 2010).

465 – ~~experiment versus~~ Experiment Versus DNS: Experimental findings showed convincing agreement with DNS con-
ducted under similar thermodynamic conditions, marking a rare comparative analysis in this field. Velocity profiles
supported the argument for the nature of thermal plumes, and a method to convert spectra from the frequency domain
to the wavenumber domain was detailed (see Appendix C). Despite the presence of imperfect boundaries such as win-
dow flanges, sampling ports, and instrumentation, idealized DNS provided a reasonable representation of the actual Π
Chamber flow, indicating that DNS adequately resolves surface layer fluxes. These results are valuable for improving
470 and validating numerical research, such as sub-grid Large-Eddy Simulation models (Salesky et al., 2024), as well as
~~global and local~~ heat transport models (Seheel et al., 2013)(Goluskin, 2015).

Data availability. The measurement records collected within this study are available from the authors upon request.

Appendix A: Quicklooks of temperature fluctuations

475 The figures illustrate ~~the maximum local~~ two realizations of temperature fluctuations at the sensor's position under similar
conditions (from the experiment and DNS). The presence of filaments or coherent structures, with temperatures close to that
of the nearby plate, is clearly visible. Note that this is not one-to-one comparison of the same flow.

Appendix B: Non-dimensional representation of standard deviations

Non-dimensionalized profiles of the standard deviation show stronger convergence in longer records ~~and display greater~~
~~symmetry~~ compared to their dimensional representation.

480 Appendix C: Power Spectral Density in wavenumber space

In the atmospheric community, PSD is typically presented in either the frequency or wavenumber domain, depending on
preferences or scientific goals. As demonstrated in Section 3.2, the collapsed spectral curves in the frequency domain exhibit
three dynamic regimes that characterize thermal convection in the Π Chamber. However, by following the scaling method
proposed by Kumar and Verma (2018) and the generalized approach of Zhou and Xia (2001), one can obtain analogous PSD
485 in the wavenumber domain.

The first step of the scaling procedure involves the following transformations:

$$k \approx \tilde{f} = f(2\pi)/U,$$

$$P(k) \approx P(\tilde{f}) = P(f)U/2\pi.$$

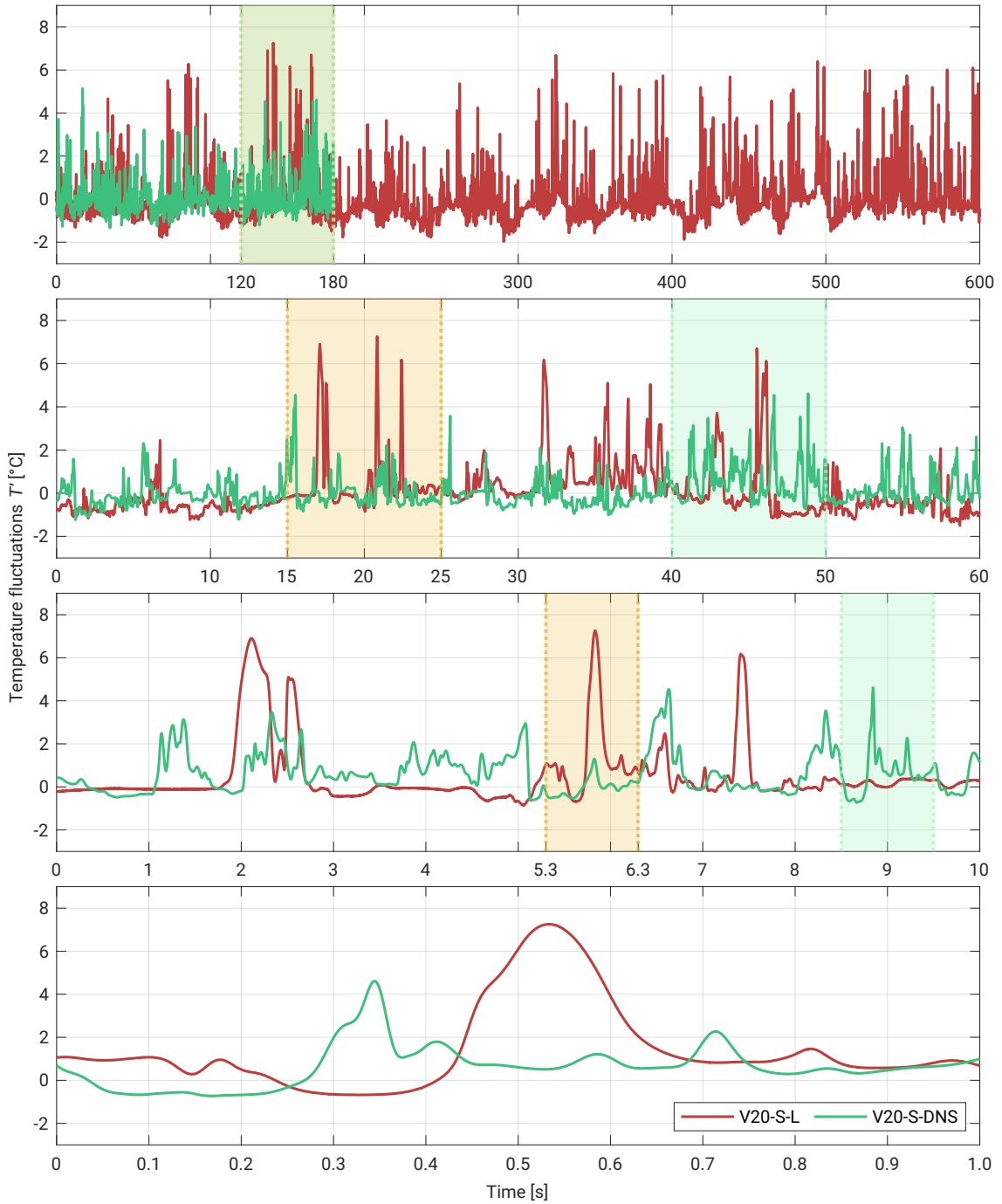


Figure A1. Experimental versus DNS T' series ~ 8 cm above the floor showed in the following zoomed in time segments: 600 s, 60 s, 10 s, and 1 s. The used dataset covers $\Delta T = 20$ K case.



Figure A2. Experimental versus DNS T' series ~ 5 cm below the ceiling showed in the following zoomed in time segments: 600 s, 60 s, 10 s, and 1 s. The used dataset covers $\Delta T = 20$ K case.

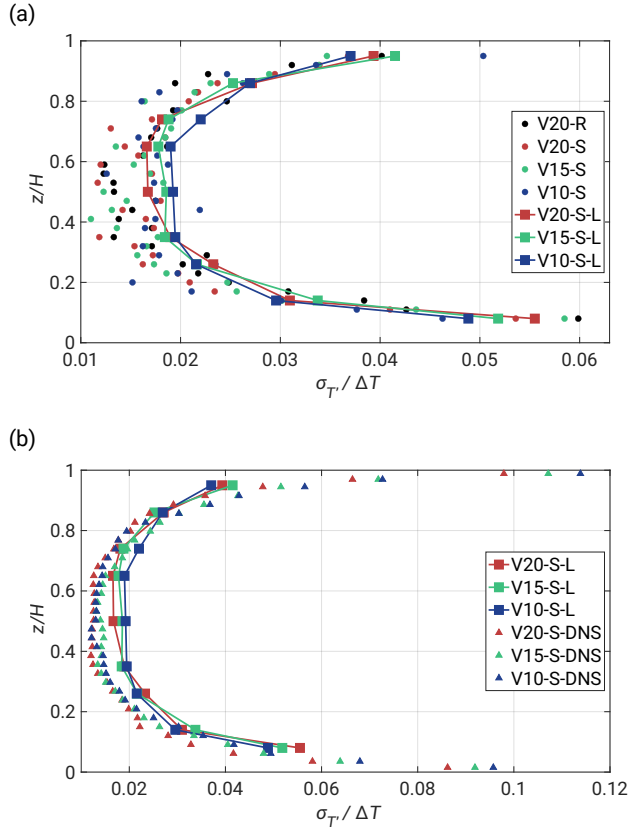


Figure B1. Non-dimensionalized standard deviation scaled by corresponding ΔT . In the figure z/H represents vertical distance z measured from the bottom plate being normalized by the cell height $H = 1$ m. (a) Analogy of Fig. 5. (b) Analogy of Fig. 11.

where $P(\tilde{f})$ and \tilde{f} represent the scaled frequency spectrum and scaled frequency, respectively. The DNS data revealed a symmetrical profile of the mean velocity U near the axis (see Fig. C1). It gradually decreases towards the bulk region, reaching 490 about 0.02 m/s, and maintains approximately equal values near both plates. The resulting wavenumber spectral curves are rescaled with U and shifted accordingly. To collapse them, we found the Kolmogorov length scale, defined as $\eta = (2\pi)/k_n$, where k_n is the wavenumber noise level, and performed another scaling to obtain the $P(\eta k)$ spectrum. The last step follows the adopted procedure of Zhou and Xia (2001).

In Fig. C2a, we present the estimation of $k_p\eta$, what is a direct analogy to f_p in Subsection 3.2, for the V20-S-L case in 495 the scaled $k\eta^2 P(k\eta)$ spectrum. Unlike the corresponding plot in the frequency domain (see Fig. 8a), $k_p\eta$ does not oscillate around one value. Here, we observe a gradual increase in $k_p\eta$ values towards the bulk region, with the $k\eta^2 P(k\eta)$ maximum occurring around $k_p\eta \approx 1/10$, which is in agreement with Monin and Yaglom (1975) (see Subsection 23.4 and Fig. 77). Fig. C2b provides the final result of the frequency to wavenumber scaling. Both the slopes and dynamic ranges are conserved, providing a clear analogy to Fig. 8.

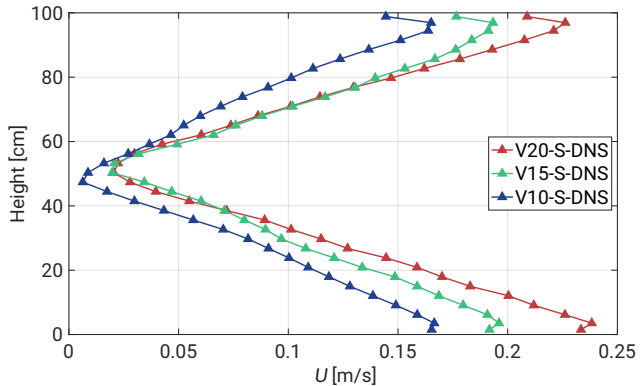


Figure C1. Mean-Magnitude of the mean velocity U profile near the axis of the chamber with respect to its height. Each curve represent different ΔT .

500 **Appendix D: Standard deviation scaling**

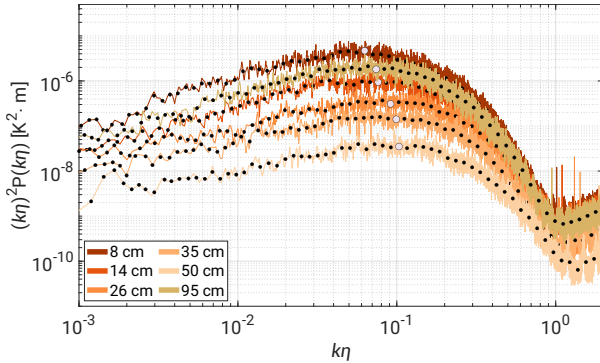
To verify if and where we can observe thermal plume dominance in the chamber, we followed the methodology outlined by He and Xia (2019). They demonstrated a strong connection between plumes and the logarithmic root mean square temperature profile using a different setup, which consisted of water as a working fluid ($\text{Pr} = 4.34$), a rectangular-shaped container with $\Gamma = 4.2$, and Ra varied from 3.2×10^7 to 2×10^8 . For our purposes, we analyzed the standard deviation $\sigma_{T'}$ distribution of 505 both the 19 min, 3 min, and DNS datasets. Fig. D1 displays presents the results for regions near both plates along with the respective Pearson correlation coefficients two regions in the semi-log domain. We selected regions approximately ~ 15 –35 cm near the floor (Fig. D1a) and ~ 65 –95 cm near the ceiling (Fig. D1b). In the both regimes we provided the respective Pearson correlation coefficients and fitted the curves for 19 min time series.

Each profile in the lower half of the chamber exhibits significant linearity correlation in the given region, including the 510 3 min experimental dataset. Only the V10-S case notably differs from the remaining results, dropping down to $p = -0.59$. The corresponding area in the upper half gives similarly high indications of the p values, excluding shorter measurements, providing evidence of weaker thermal plume response. This observation is reasonable considering the previous discussion in Sec. 3.1 on differences between both regions of the cell.

It is worth mentioning that the zones outside the selected profiles are clearly dominated by different types of forces, resulting 515 in very local dynamics in the RBC.

Author contributions. RG, RAS, JCA, WC, and SPM designed the study. RG and JCA adapted the UFT instrument and the II Chamber facility for the measurements. RG and JCA performed the UFT measurements. KKC performed DNS. RG processed and analysed the collected data with advice from RAS, SPM, and KKC. RG wrote the manuscript with contributions from RAS, SPM and KKC (who wrote Subsection 2.2). All authors critically proofread and revised the manuscript.

(a)



(b)

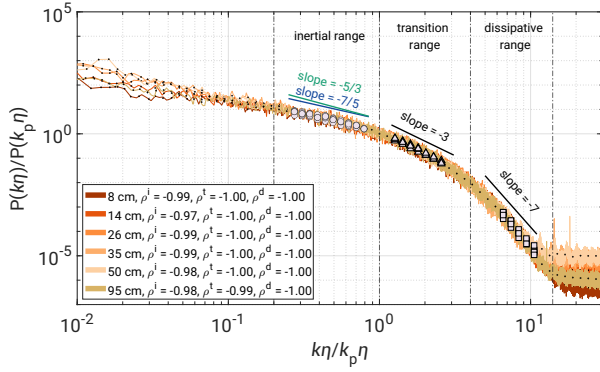


Figure C2. Analogical to Fig. 8 spectra of V20-S-L case but in wavenumber domain. **(a)** Scaled spectrum of $k\eta^2 P(k\eta)$. **(b)** PSD $P(k\eta)/P(k_p\eta)$ versus $k\eta/k_p\eta$ with three defined regimes: inertial range (circles, $0.2 \leq k\eta/k_p\eta \leq 1$), transition range (triangles, $1 \leq k\eta/k_p\eta \leq 4$), and dissipative range (squares, $4 \leq k\eta/k_p\eta \leq 20$). Legend includes the Pearson correlation coefficients p .

520 RG is truly grateful to Marta Wacławczyk and Jun-Ichi Yano for thought-provoking talks and for providing constructive feedback on our work.

Competing interests. The authors have the following competing interests: Szymon P. Malinowski is a member of the editorial board of Atmospheric Measurement Techniques.

525 *Acknowledgements.* This project has received funding from the Excellence Initiative-Research University Programme (IDUB) as part of Action IV.4.1 under grant agreement No. BOB-IDUB-622-913/2023.

J. C. Anderson, W. Cantrell, and R. A. Shaw acknowledge support from the U.S. National Science Foundation through grant No. AGS-2113060.

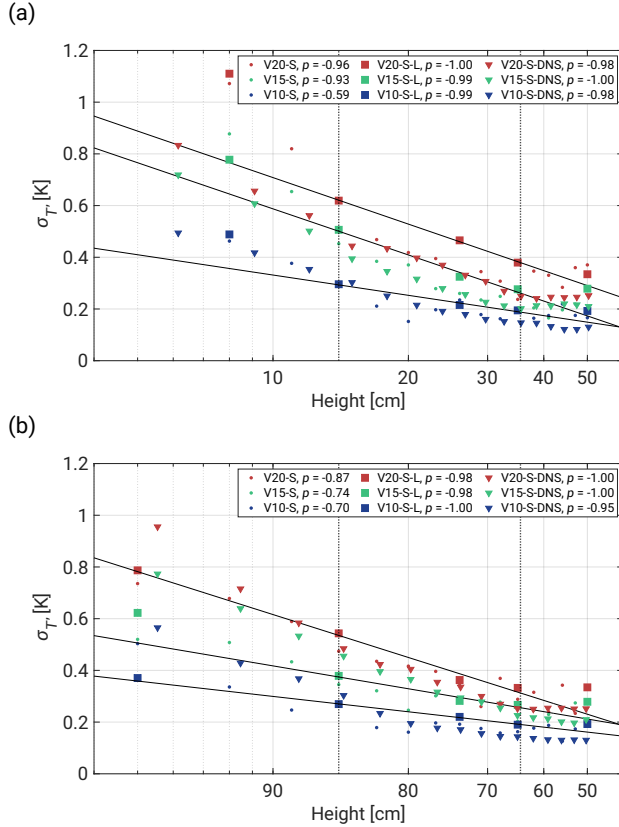


Figure D1. Standard deviation $\sigma_{T'}$ distribution of both 19 min, 3 min and DNS dataset in semi-log domain near the floor (a) and close to the ceiling (b). [Fitted](#) Both legends include Pearson correlation coefficients. Note that the [fitted](#) curves correspond [only](#) with 19 min measurements. [Both legends include Pearson correlation coefficients](#).

K. K. Chandrakar's contribution was supported by the NSF National Center for Atmospheric Research, which is a major facility sponsored by the U.S. National Science Foundation under Cooperative Agreement No. 1852977.

530 **References**

Ahlers, G., Bodenschatz, E., Hartmann, R., He, X., Lohse, D., Reiter, P., Stevens, R. J. A. M., Verzicco, R., Wedi, M., Weiss, S., Zhang, X., Zwirner, L., and Shishkina, O.: Aspect Ratio Dependence of Heat Transfer in a Cylindrical Rayleigh–Bénard Cell, *Phys. Rev. Lett.*, 128, 084501, <https://doi.org/10.1103/PhysRevLett.128.084501>, 2022.

Alexakis, A.: Quasi-two-dimensional turbulence, *Reviews of Modern Plasma Physics*, 7, 31, <https://doi.org/10.1007/s41614-023-00134-3>, 535 2023.

Alexakis, A. and Biferale, L.: Cascades and transitions in turbulent flows, *Physics Reports*, 767–769, 1–101, <https://doi.org/https://doi.org/10.1016/j.physrep.2018.08.001>, cascades and transitions in turbulent flows, 2018.

Anderson, J. C., Thomas, S., Prabhakaran, P., Shaw, R. A., and Cantrell, W.: Effects of the large-scale circulation on temperature and water vapor distributions in the II Chamber, *Atmospheric Measurement Techniques*, 14, 5473–5485, <https://doi.org/10.5194/AMT-14-5473-540>, 2021, 2021.

Ashkenazi, S. and Steinberg, V.: Spectra and Statistics of Velocity and Temperature Fluctuations in Turbulent Convection, *Phys. Rev. Lett.*, 83, 4760–4763, <https://doi.org/10.1103/PhysRevLett.83.4760>, 1999.

Bailon-Cuba, J., Emran, M. S., and Schumacher, J.: Aspect ratio dependence of heat transfer and large-scale flow in turbulent convection, *Journal of Fluid Mechanics*, 655, 152–173, <https://doi.org/10.1017/S0022112010000820>, 2010.

545 Batchelor, G. K.: Small-scale variation of convected quantities like temperature in turbulent fluid Part 1. General discussion and the case of small conductivity, *Journal of Fluid Mechanics*, 5, 113–133, <https://doi.org/10.1017/S002211205900009X>, 1959.

Blass, A., Verzicco, R., Lohse, D., Stevens, R. J. A. M., and Krug, D.: Flow organisation in laterally unconfined Rayleigh–Bénard turbulence, *Journal of Fluid Mechanics*, 906, A26, <https://doi.org/10.1017/jfm.2020.797>, 2021.

Brown, E. and Ahlers, G.: Large-Scale Circulation Model for Turbulent Rayleigh–Bénard Convection, *Phys. Rev. Lett.*, 98, 134501, 550 <https://doi.org/10.1103/PhysRevLett.98.134501>, 2007.

Brown, E. and Ahlers, G.: The origin of oscillations of the large-scale circulation of turbulent Rayleigh–Bénard convection, *Journal of Fluid Mechanics*, 638, 383–400, <https://doi.org/10.1017/S0022112009991224>, 2009.

Bryan, G. H. and Fritsch, J. M.: A benchmark simulation for moist nonhydrostatic numerical models, *Monthly Weather Review*, 130, 2917–2928, 2002.

555 Buaria, D. and Sreenivasan, K. R.: Dissipation range of the energy spectrum in high Reynolds number turbulence, *Phys. Rev. Fluids*, 5, 092601, <https://doi.org/10.1103/PhysRevFluids.5.092601>, 2020.

Castaing, B.: Scaling of turbulent spectra, *Phys. Rev. Lett.*, 65, 3209–3209, <https://doi.org/10.1103/PhysRevLett.65.3209>, 1990.

Cencini, M., Muratore-Ginanneschi, P., and Vulpiani, A.: Nonlinear Superposition of Direct and Inverse Cascades in Two-Dimensional Turbulence Forced at Large and Small Scales, *Phys. Rev. Lett.*, 107, 174502, <https://doi.org/10.1103/PhysRevLett.107.174502>, 2011.

560 Chandrakar, K. K., Cantrell, W., Kostinski, A. B., and Shaw, R. A.: Dispersion Aerosol Indirect Effect in Turbulent Clouds: Laboratory Measurements of Effective Radius, *Geophysical Research Letters*, 45, 10,738–10,745, <https://doi.org/https://doi.org/10.1029/2018GL079194>, 2018a.

Chandrakar, K. K., Cantrell, W., and Shaw, R. A.: Influence of Turbulent Fluctuations on Cloud Droplet Size Dispersion and Aerosol Indirect Effects, *Journal of the Atmospheric Sciences*, 75, 3191–3209, <https://doi.org/10.1175/JAS-D-18-0006.1>, 2018b.

565 Chandrakar, K. K., Saito, I., Yang, F., Cantrell, W., Gotoh, T., and Shaw, R. A.: Droplet size distributions in turbulent clouds: experimental evaluation of theoretical distributions, *Quarterly Journal of the Royal Meteorological Society*, 146, 483–504, <https://doi.org/https://doi.org/10.1002/qj.3692>, 2020.

Chandrakar, K. K., Morrison, H., Grabowski, W. W., Bryan, G. H., and Shaw, R. A.: Supersaturation Variability from Scalar Mixing: Evaluation of a New Subgrid-Scale Model Using Direct Numerical Simulations of Turbulent Rayleigh–Bénard Convection, *Journal of the Atmospheric Sciences*, 79, 1191–1210, <https://doi.org/https://doi.org/10.1175/JAS-D-21-0250.1>, 2022.

570 Chandrakar, K. K., Morrison, H., and Shaw, R. A.: Lagrangian and Eulerian Supersaturation Statistics in Turbulent Cloudy Rayleigh–Bénard Convection: Applications for LES Subgrid Modeling, *Journal of the Atmospheric Sciences*, 80, 2261–2285, <https://doi.org/https://doi.org/10.1175/JAS-D-22-0256.1>, 2023.

Chang, K., Bench, J., Brege, M., Cantrell, W., Chandrakar, K., Ciochetto, D., Mazzoleni, C., Mazzoleni, L. R., Niedermeier, D., and Shaw, 575 R. A.: A Laboratory Facility to Study Gas–Aerosol–Cloud Interactions in a Turbulent Environment: The II Chamber, *Bulletin of the American Meteorological Society*, 97, 2343–2358, <https://doi.org/10.1175/BAMS-D-15-00203.1>, 2016.

Chen, C. H. and Bhaganagar, K.: New findings in vorticity dynamics of turbulent buoyant plumes, *Physics of Fluids*, 33, 115 104, <https://doi.org/10.1063/5.0065322>, 2021.

Chen, C. H. and Bhaganagar, K.: Energetics of buoyancy-generated turbulent flows with active scalar: pure buoyant plume, *Journal of Fluid Mechanics*, 954, A23, <https://doi.org/10.1017/jfm.2022.1011>, 2023.

580 Chen, C. H. and Bhaganagar, K.: Turbulent cascading in Buoyant plumes, *Environmental Fluid Mechanics*, <https://doi.org/10.1007/s10652-023-09963-9>, 2024.

Chen, J., Yin, Z.-X., and Zou, H.-Y.: Visualization of thermal structures in turbulent Rayleigh–Bénard convection, in: *Proceedings 18th International Symposium on Flow Visualization*, ETH Zurich, 2018.

585 Chillà, F. and Schumacher, J.: New perspectives in turbulent Rayleigh–Bénard convection, *The European Physical Journal E*, 35, 58, <https://doi.org/10.1140/epje/i2012-12058-1>, 2012.

Chillà, F., Ciliberto, S., Innocenti, C., and Pampaloni, E.: Boundary layer and scaling properties in turbulent thermal convection, *Il Nuovo Cimento D*, 15, 1229–1249, <https://doi.org/10.1007/BF02451729>, 1993.

Cioni, S., Ciliberto, S., and Sommeria, J.: Temperature Structure Functions in Turbulent Convection at Low Prandtl Number, *Europhysics Letters*, 32, 413, <https://doi.org/10.1209/0295-5075/32/5/006>, 1995.

590 Dabbagh, F., Trias, F. X., Gorobets, A., and Oliva, A.: Flow topology dynamics in a three-dimensional phase space for turbulent Rayleigh–Bénard convection, *Phys. Rev. Fluids*, 5, 024 603, <https://doi.org/10.1103/PhysRevFluids.5.024603>, 2020.

De, A. K., Eswaran, V., and Mishra, P. K.: Dynamics of plumes in turbulent Rayleigh–Bénard convection, *European Journal of Mechanics - B/Fluids*, 72, 164–178, <https://doi.org/https://doi.org/10.1016/j.euromechflu.2018.05.007>, 2018.

595 de la Torre Juárez, M., Chavez, A., Tamppari, L. K., Munguira, A., Martínez, G., Hueso, R., Chide, B., Murdoch, N., Stott, A. E., Navarro, S., Sánchez-Lavega, A., Orton, G. S., Viúdez-Moreiras, D., Banfield, D. J., and Rodríguez-Manfredi, J. A.: Diurnal Cycle of Rapid Air Temperature Fluctuations at Jezero Crater: Probability Distributions, Exponential Tails, Scaling, and Intermittency, *Journal of Geophysical Research: Planets*, 128, e2022JE007458, <https://doi.org/https://doi.org/10.1029/2022JE007458>, e2022JE007458 2022JE007458, 2023.

de Wit, X. M., van Kan, A., and Alexakis, A.: Bistability of the large-scale dynamics in quasi-two-dimensional turbulence, *Journal of Fluid Mechanics*, 939, R2, <https://doi.org/10.1017/jfm.2022.209>, 2022.

600 Desai, N., Chandrakar, K. K., Chang, K., Cantrell, W., and Shaw, R. A.: Influence of Microphysical Variability on Stochastic Condensation in a Turbulent Laboratory Cloud, *Journal of the Atmospheric Sciences*, 75, 189 – 201, <https://doi.org/10.1175/JAS-D-17-0158.1>, 2018.

Desai, N., Chandrakar, K. K., Kinney, G., Cantrell, W., and Shaw, R. A.: Aerosol-Mediated Glaciation of Mixed-Phase Clouds: Steady-State Laboratory Measurements, *Geophysical Research Letters*, 46, 9154–9162, [https://doi.org/https://doi.org/10.1029/2019GL083503](https://doi.org/10.1029/2019GL083503), 2019.

605 du Puits, R.: Time-resolved measurements of the local wall heat flux in turbulent Rayleigh–Bénard convection, *International Journal of Heat and Mass Transfer*, 188, 122 649, [https://doi.org/https://doi.org/10.1016/j.ijheatmasstransfer.2022.122649](https://doi.org/10.1016/j.ijheatmasstransfer.2022.122649), 2022.

du Puits, R.: Thermal boundary layers in turbulent Rayleigh–Bénard convection with rough and smooth plates: A one-to-one comparison, *Phys. Rev. Fluids*, 9, 023 501, <https://doi.org/10.1103/PhysRevFluids.9.023501>, 2024.

610 du Puits, R., Resagk, C., and Thess, A.: Thermal boundary layers in turbulent Rayleigh–Bénard convection at aspect ratios between 1 and 9, *New Journal of Physics*, 15, 013 040, <https://doi.org/10.1088/1367-2630/15/1/013040>, 2013.

Eidelman, A., Elperin, T., Gluzman, I., and Golbraikh, E.: Helicity of mean and turbulent flow with coherent structures in Rayleigh–Bénard convective cell, *Physics of Fluids*, 26, 065 103, <https://doi.org/10.1063/1.4881939>, 2014.

615 Fan, Y., Zhao, Y., Torres, J. F., Xu, F., Lei, C., Li, Y., and Carmeliet, J.: Natural convection over vertical and horizontal heated flat surfaces: A review of recent progress focusing on underpinnings and implications for heat transfer and environmental applications, *Physics of Fluids*, 33, 101 301, <https://doi.org/10.1063/5.0065125>, 2021.

Fernando, H. and Smith IV, D.: Vortex structures in geophysical convection, *European Journal of Mechanics - B/Fluids*, 20, 437–470, [https://doi.org/https://doi.org/10.1016/S0997-7546\(01\)01129-3](https://doi.org/10.1016/S0997-7546(01)01129-3), 2001.

620 Foroozani, N., Niemela, J. J., Armenio, V., and Sreenivasan, K. R.: Reorientations of the large-scale flow in turbulent convection in a cube, *Phys. Rev. E*, 95, 033 107, <https://doi.org/10.1103/PhysRevE.95.033107>, 2017.

Funfschilling, D., Brown, E., and Ahlers, G.: Torsional oscillations of the large-scale circulation in turbulent Rayleigh–Bénard convection, *Journal of Fluid Mechanics*, 607, 119–139, <https://doi.org/10.1017/S0022112008001882>, 2008.

Goluskin, D.: Internally Heated Convection and Rayleigh–Bénard Convection, *SpringerBriefs in Applied Sciences and Technology*, Springer International Publishing, ISBN 9783319239415, <https://doi.org/10.1007/978-3-319-23941-5>, 2015.

625 Gotoh, T. and Yeung, P.: Ten Chapters in Turbulence, p. 87–131, Cambridge University Press, <https://doi.org/10.1017/CBO9781139032810>, 2012.

Guo, S.-X., Zhou, S.-Q., Qu, L., Cen, X.-R., and Lu, Y.-Z.: Evolution and statistics of thermal plumes in tilted turbulent convection, *International Journal of Heat and Mass Transfer*, 111, 933–942, <https://doi.org/https://doi.org/10.1016/j.ijheatmasstransfer.2017.04.039>, 2017.

Haman, K. E., Makulski, A., Malinowski, S. P., and Busen, R.: A new ultrafast thermometer for airborne measurements in clouds, *Journal of Atmospheric and Oceanic Technology*, 14, 217–227, [https://doi.org/10.1175/1520-0426\(1997\)014<0217:ANUTFA>2.0.CO;2](https://doi.org/10.1175/1520-0426(1997)014<0217:ANUTFA>2.0.CO;2), 1997.

630 Haman, K. E., Malinowski, S. P., and Struś, B. D.: Two new types of ultrafast aircraft thermometer, *Journal of Atmospheric and Oceanic Technology*, 18, 117–134, <https://doi.org/10.1175/1520-0426>, 2001.

He, X., van Gils, D. P. M., Bodenschatz, E., and Ahlers, G.: Logarithmic Spatial Variations and Universal f^{-1} Power Spectra of Temperature Fluctuations in Turbulent Rayleigh–Bénard Convection, *Phys. Rev. Lett.*, 112, 174 501, <https://doi.org/10.1103/PhysRevLett.112.174501>, 2014.

635 He, X., Wang, Y., and Tong, P.: Dynamic heterogeneity and conditional statistics of non-Gaussian temperature fluctuations in turbulent thermal convection, *Phys. Rev. Fluids*, 3, 052 401, <https://doi.org/10.1103/PhysRevFluids.3.052401>, 2018.

He, Y.-H. and Xia, K.-Q.: Temperature Fluctuation Profiles in Turbulent Thermal Convection: A Logarithmic Dependence versus a Power-Law Dependence, *Phys. Rev. Lett.*, 122, 014 503, <https://doi.org/10.1103/PhysRevLett.122.014503>, 2019.

Khurshid, S., Donzis, D. A., and Sreenivasan, K. R.: Energy spectrum in the dissipation range, *Phys. Rev. Fluids*, 3, 082 601, <https://doi.org/10.1103/PhysRevFluids.3.082601>, 2018.

640

Kraichnan, R. H.: Inertial Ranges in Two-Dimensional Turbulence, *The Physics of Fluids*, 10, 1417–1423, <https://doi.org/10.1063/1.1762301>, 1967.

Kraichnan, R. H.: Small-Scale Structure of a Scalar Field Convected by Turbulence, *The Physics of Fluids*, 11, 945–953, <https://doi.org/10.1063/1.1692063>, 1968.

645 Krug, D., Lohse, D., and Stevens, R. J. A. M.: Coherence of temperature and velocity superstructures in turbulent Rayleigh–Bénard flow, *Journal of Fluid Mechanics*, 887, A2, <https://doi.org/10.1017/jfm.2019.1054>, 2020.

Kukharets, V. P. and Nalbandyan, H. G.: Temperature fluctuations in the atmospheric surface layer over the thermally inhomogeneous underlying surface, *Izvestiya, Atmospheric and Oceanic Physics*, 42, 456–462, <https://doi.org/10.1134/S0001433806040050>, 2006.

650 Kumala, W., Haman, K. E., Kopec, M. K., Khelif, D., and Malinowski, S. P.: Modified ultrafast thermometer UFT-M and temperature measurements during Physics of Stratocumulus Top (POST), *Atmospheric Measurement Techniques*, 6, 2043–2054, <https://doi.org/10.5194/amt-6-2043-2013>, 2013.

Kumar, A. and Verma, M. K.: Applicability of Taylor's hypothesis in thermally driven turbulence, *Royal Society Open Science*, 5, 172 152, <https://doi.org/10.1098/rsos.172152>, 2018.

Lakkaraju, R., Stevens, R. J. A. M., Verzicco, R., Grossmann, S., Prosperetti, A., Sun, C., and Lohse, D.: Spatial distribution of heat flux and 655 fluctuations in turbulent Rayleigh–Bénard convection, *Phys. Rev. E*, 86, 056 315, <https://doi.org/10.1103/PhysRevE.86.056315>, 2012.

Lenschow, D. H., Mann, J., and Kristensen, L.: How Long Is Long Enough When Measuring Fluxes and Other Turbulence Statistics?, *Journal of Atmospheric and Oceanic Technology*, 11, 661–673, [https://doi.org/https://doi.org/10.1175/1520-0426\(1994\)011<0661:HLILEW>2.0.CO;2](https://doi.org/https://doi.org/10.1175/1520-0426(1994)011<0661:HLILEW>2.0.CO;2), 1994.

Liu, Y. and Ecke, R. E.: Local temperature measurements in turbulent rotating Rayleigh–Bénard convection, *Phys. Rev. E*, 84, 016 311, 660 <https://doi.org/10.1103/PhysRevE.84.016311>, 2011.

Lohse, D. and Shishkina, O.: Ultimate Rayleigh–Bénard turbulence, *Rev. Mod. Phys.*, 96, 035 001, <https://doi.org/10.1103/RevModPhys.96.035001>, 2024.

Lohse, D. and Xia, K.-Q.: Small-Scale Properties of Turbulent Rayleigh–Bénard Convection, *Annual Review of Fluid Mechanics*, 42, 335–364, <https://doi.org/https://doi.org/10.1146/annurev.fluid.010908.165152>, 2010.

665 MacMillan, T., Shaw, R. A., Cantrell, W. H., and Richter, D. H.: Direct numerical simulation of turbulence and microphysics in the Pi Chamber, *Phys. Rev. Fluids*, 7, 020 501, <https://doi.org/10.1103/PhysRevFluids.7.020501>, 2022.

Mishra, P. K., De, A. K., Verma, M. K., and Eswaran, V.: Dynamics of reorientations and reversals of large-scale flow in Rayleigh–Bénard convection, *Journal of Fluid Mechanics*, 668, 480–499, <https://doi.org/10.1017/S0022112010004830>, 2011.

Moller, S., Resagk, C., and Cierpka, C.: Long-time experimental investigation of turbulent superstructures in Rayleigh–Bénard convection by 670 noninvasive simultaneous measurements of temperature and velocity fields, *Experiments in Fluids*, 62, 64, <https://doi.org/10.1007/s00348-020-03107-1>, 2021.

Monin, A. and Yaglom, A.: *Statistical Fluid Mechanics, Volume II: Mechanics of Turbulence*, The MIT Press, 1975.

Musacchio, S. and Boffetta, G.: Condensate in quasi-two-dimensional turbulence, *Phys. Rev. Fluids*, 4, 022 602, <https://doi.org/10.1103/PhysRevFluids.4.022602>, 2019.

675 Niedermeier, D., Chang, K., Cantrell, W., Chandrakar, K. K., Ciochetto, D., and Shaw, R. A.: Observation of a link between energy dissipation rate and oscillation frequency of the large-scale circulation in dry and moist Rayleigh–Bénard turbulence, *Phys. Rev. Fluids*, 3, 083 501, <https://doi.org/10.1103/PhysRevFluids.3.083501>, 2018.

Niemela, J. J., Skrbek, L., Sreenivasan, K. R., and Donnelly, R. J.: Turbulent convection at very high Rayleigh numbers, *Nature*, 404, 837–840, <https://doi.org/10.1038/35009036>, 2000.

680 Nowak, J., Kumala, W., Kwiatkowski, A., Kwiatkowski, K., Czyżewska, D., Karpińska, K., and Malinowski, S.: UltraFast Thermometer 2.0 - new temperature sensor for airborne applications and its performance during ACORES 2017, *Geophysical Research Abstracts*, <https://doi.org/10.13140/RG.2.2.12500.24967>, 2018.

Nowak, J. L., Siebert, H., Szodry, K.-E., and Malinowski, S. P.: Coupled and decoupled stratocumulus-topped boundary layers: turbulence properties, *Atmospheric Chemistry and Physics Discussions*, 2021, 1–41, <https://doi.org/10.5194/acp-2021-214>, 2021.

685 Olsthoorn, J.: Accounting for surface temperature variations in Rayleigh-Bénard convection, *Phys. Rev. Fluids*, 8, 033501, <https://doi.org/10.1103/PhysRevFluids.8.033501>, 2023.

Pandey, A., Scheel, J. D., and Schumacher, J.: Turbulent superstructures in Rayleigh-Bénard convection, *Nature Communications*, 9, 2118, <https://doi.org/10.1038/s41467-018-04478-0>, 2018.

690 Pawar, S. S. and Arakeri, J. H.: Kinetic energy and scalar spectra in high Rayleigh number axially homogeneous buoyancy driven turbulence, *Physics of Fluids*, 28, 065103, <https://doi.org/10.1063/1.4953858>, 2016.

Plunian, F., Teimurazov, A., Stepanov, R., and Verma, M. K.: Inverse cascade of energy in helical turbulence, *Journal of Fluid Mechanics*, 895, A13, <https://doi.org/10.1017/jfm.2020.307>, 2020.

695 Prabhakaran, P., Shawon, A. S. M., Kinney, G., Thomas, S., Cantrell, W., and Shaw, R. A.: The role of turbulent fluctuations in aerosol activation and cloud formation, *Proceedings of the National Academy of Sciences*, 117, 16831–16838, <https://doi.org/10.1073/pnas.2006426117>, 2020.

Reiter, P., Shishkina, O., Lohse, D., and Krug, D.: Crossover of the relative heat transport contributions of plume ejecting and impacting zones in turbulent Rayleigh-Bénard convection(a), *Europhysics Letters*, 134, 34002, <https://doi.org/10.1209/0295-5075/134/34002>, 2021.

Rieutord, M., Roudier, T., Rincon, F., Malherbe, J.-M., Meunier, N., Berger, T., and Frank, Z.: On the power spectrum of solar surface flows, *A&A*, 512, A4, <https://doi.org/10.1051/0004-6361/200913303>, 2010.

700 Sakievich, P., Peet, Y., and Adrian, R.: Large-scale thermal motions of turbulent Rayleigh-Bénard convection in a wide aspect-ratio cylindrical domain, *International Journal of Heat and Fluid Flow*, 61, <https://doi.org/10.1016/j.ijheatfluidflow.2016.04.011>, 2016.

Salesky, S. T., Gillis, K., Anderson, J., Helman, I., Cantrell, W., and Shaw, R. A.: Modeling the subgrid scale scalar variance: a priori tests and application to supersaturation in cloud turbulence, *Journal of the Atmospheric Sciences*, <https://doi.org/10.1175/JAS-D-23-0163.1>, 2024.

705 Scheel, J. D., Emran, M. S., and Schumacher, J.: Resolving the fine-scale structure in turbulent Rayleigh-Bénard convection, *New Journal of Physics*, 15, 113063, <https://doi.org/10.1088/1367-2630/15/11/113063>, 2013.

Shevkar, P. P., Vishnu, R., Mohanan, S. K., Koothur, V., Mathur, M., and Puthenveettil, B. A.: On separating plumes from boundary layers in turbulent convection, *Journal of Fluid Mechanics*, 941, A5, <https://doi.org/DOI: 10.1017/jfm.2022.271>, 2022.

710 Shi, N., Emran, M. S., and Schumacher, J.: Boundary layer structure in turbulent Rayleigh-Bénard convection, *Journal of Fluid Mechanics*, 706, 5–33, <https://doi.org/DOI: 10.1017/jfm.2012.207>, 2012.

Shishkina, O.: Rayleigh-Bénard convection: The container shape matters, *Phys. Rev. Fluids*, 6, 090502, <https://doi.org/10.1103/PhysRevFluids.6.090502>, 2021.

Shishkina, O., Horn, S., Emran, M. S., and Ching, E. S. C.: Mean temperature profiles in turbulent thermal convection, *Phys. Rev. Fluids*, 2, 113502, <https://doi.org/10.1103/PhysRevFluids.2.113502>, 2017.

715 Siebert, H., Lehmann, K., and Wendisch, M.: Observations of small-scale turbulence and energy dissipation rates in the cloudy boundary layer, *Journal of the Atmospheric Sciences*, 63, 1451–1466, <https://doi.org/10.1175/JAS3687.1>, 2006.

720 Siebert, H., Szodry, K. E., Egerer, U., Wehner, B., Henning, S., Chevalier, K., Lückerath, J., Welz, O., Weinhold, K., Lauermann, F., Gottschalk, M., Ehrlich, A., Wendisch, M., Fialho, P., Roberts, G., Allwayin, N., Schum, S., Shaw, R. A., Mazzoleni, C., Mazzoleni, L., Nowak, J. L., Malinowski, S. P., Karpinska, K., Kumala, W., Czyzewska, D., Luke, E. P., Kollias, P., Wood, R., and Mellado, J. P.: Observations of aerosol, cloud, turbulence, and radiation properties at the top of the Marine Boundary Layer over the Eastern North Atlantic Ocean: The ACORES Campaign, *Bulletin of the American Meteorological Society*, 102, E123–E147, <https://doi.org/10.1175/BAMS-D-19-0191.1>, 2021.

Sreenivasan, K. R.: Turbulent mixing: A perspective, *Proceedings of the National Academy of Sciences*, 116, 18 175–18 183, <https://doi.org/10.1073/pnas.1800463115>, 2019.

725 Stevens, B., Bony, S., Farrell, D., Ament, F., Blyth, A., Fairall, C., Karstensen, J., Quinn, P. K., Speich, S., Acquistapace, C., Aemisegger, F., Albright, A. L., Bellenger, H., Bodenschatz, E., Caesar, K. A., Chewitt-Lucas, R., De Boer, G., Delanoë, J., Denby, L., Ewald, F., Fildier, B., Forde, M., George, G., Gross, S., Hagen, M., Hausold, A., Heywood, K. J., Hirsch, L., Jacob, M., Jansen, F., Kinne, S., Klocke, D., Kölling, T., Konow, H., Lothon, M., Mohr, W., Naumann, A. K., Nuijens, L., Olivier, L., Pincus, R., Pöhlker, M., Reverdin, G., Roberts, G., Schnitt, S., Schulz, H., Pier Siebesma, A., Stephan, C. C., Sullivan, P., Touzé-Peiffer, L., Vial, J., Vogel, R., Zuidema, P., Alexander, N., Alves, L., Aixi, S., Asmath, H., Bagheri, G., Baier, K., Bailey, A., Baranowski, D., Baron, A., Barrau, S., Barrett, P. A., Batier, F., Behrendt, A., Bendinger, A., Beucher, F., Bigorre, S., Blades, E., Blossey, P., Bock, O., Böing, S., Bosser, P., Bourras, D., Bouruet-Aubertot, P., Bower, K., Branellec, P., Branger, H., Brennek, M., Brewer, A., Brilouet, P. E., Brügmann, B., Buehler, S. A., Burke, E., Burton, R., Calmer, R., Canonici, J. C., Carton, X., Cato, G., Charles, J. A., Chazette, P., Chen, Y., Chilinski, M. T., Choularton, T., Chuang, P., Clarke, S., Coe, H., Cornet, C., Coutris, P., Couvreux, F., Crewell, S., Cronin, T., Cui, Z., Cuypers, Y., Daley, A., Damerell, 730 G. M., Dauhut, T., Deneke, H., Desbios, J. P., Dörner, S., Donner, S., Douet, V., Drushka, K., Dütsch, M., Ehrlich, A., Emanuel, K., Emmanouilidis, A., Etienne, J. C., Etienne-Leblanc, S., Faure, G., Feingold, G., Ferrero, L., Fix, A., Flamant, C., Flatau, P. J., Foltz, G. R., Forster, L., Furtuna, I., Gadian, A., Galewsky, J., Gallagher, M., Gallimore, P., Gaston, C., Gentemann, C., Geyskens, N., Giez, A., Gollop, J., Gouirand, I., Gourbeyre, C., De Graaf, D., De Groot, G. E., Grosz, R., Güttler, J., Gutleben, M., Hall, K., Harris, G., Helfer, K. C., Henze, D., Herbert, C., Holanda, B., Ibanez-Landeta, A., Intrieri, J., Iyer, S., Julien, F., Kalesse, H., Kazil, J., Kellman, A., Kidane, A. T., 735 Kirchner, U., Klingebiel, M., Körner, M., Kremper, L. A., Kretzschmar, J., Krüger, O., Kumala, W., Kurz, A., L'Hégaret, P., Labaste, M., Lachlan-Cope, T., Laing, A., Landschützer, P., Lang, T., Lange, D., Lange, I., Laplace, C., Lavik, G., Laxenaire, R., LeBihan, C., Leandro, M., Lefevre, N., Lena, M., Lenschow, D., Li, Q., Lloyd, G., Los, S., Losi, N., Lovell, O., Luneau, C., Makuch, P., Malinowski, S., Manta, G., Marinou, E., Marsden, N., Masson, S., Maury, N., Mayer, B., Mayers-Als, M., Mazel, C., McGeary, W., McWilliams, J. C., Mech, M., Mehlmann, M., Meroni, A. N., Mieslinger, T., Minikin, A., Minnett, P., Möller, G., Avalos, Y. M., Muller, C., Musat, I., Napoli, A., Neuberger, A., Noisel, C., Noone, D., Nordsiek, F., Nowak, J. L., Oswald, L., Parker, D. J., Peck, C., Person, R., Philippi, M., Plueddemann, A., Pöhlker, C., Pörtge, V., Pöschl, U., Pologne, L., Posyniak, M., Prange, M., Meléndez, E. Q., Radtke, J., Ramage, K., Reimann, J., Renault, L., Reus, K., Reyes, A., Ribbe, J., Ringel, M., Ritschel, M., Rocha, C. B., Rochetin, N., Röttenbacher, J., Rollo, C., Royer, H., Sadoulet, P., Saffin, L., Sandiford, S., Sandu, I., Schäfer, M., Schemann, V., Schirmacher, I., Schlenczek, O., Schmidt, J., Schröder, M., Schwarzenboeck, A., Sealy, A., Senff, C. J., Serikov, I., Shohan, S., Siddle, E., Smirnov, A., Späth, F., Spooner, B., 740 Katharina Stolla, M., Szkółka, W., De Szoëke, S. P., Tarot, S., Teton, E., Thompson, E., Thomson, J., Tomassini, L., Totems, J., Ubele, A. A., Villiger, L., Von Arx, J., Wagner, T., Walther, A., Webber, B., Wendisch, M., Whitehall, S., Wiltshire, A., Wing, A. A., Wirth, M., 745 750

Wiskandt, J., Wolf, K., Worbes, L., Wright, E., Wulfmeyer, V., Young, S., Zhang, C., Zhang, D., Ziemen, F., Zinner, T., and Zöger, M.: EUREC4A, *Earth System Science Data*, 13, 4067–4119, <https://doi.org/10.5194/ESSD-13-4067-2021>, 2021.

755 Stevens, R. J. A. M., Blass, A., Zhu, X., Verzicco, R., and Lohse, D.: Turbulent thermal superstructures in Rayleigh-Bénard convection, *Phys. Rev. Fluids*, 3, 041 501, <https://doi.org/10.1103/PhysRevFluids.3.041501>, 2018.

van der Poel, E. P., Ostilla-Mónico, R., Verzicco, R., Grossmann, S., and Lohse, D.: Logarithmic Mean Temperature Profiles and Their Connection to Plume Emissions in Turbulent Rayleigh-Bénard Convection, *Phys. Rev. Lett.*, 115, 154 501, <https://doi.org/10.1103/PhysRevLett.115.154501>, 2015.

760 Vasiliev, A., Sukhanovskii, A., Frick, P., Budnikov, A., Fomichev, V., Bolshukhin, M., and Romanov, R.: High Rayleigh number convection in a cubic cell with adiabatic sidewalls, *International Journal of Heat and Mass Transfer*, 102, 201–212, <https://doi.org/https://doi.org/10.1016/j.ijheatmasstransfer.2016.06.015>, 2016.

Vishnu, V. T., De, A. K., and Mishra, P. K.: Dynamics of large-scale circulation and energy transfer mechanism in turbulent Rayleigh-Bénard convection in a cubic cell, *Physics of Fluids*, 32, 095 115, <https://doi.org/10.1063/5.0021667>, 2020.

765 Vishnu, V. T., De, A. K., and Mishra, P. K.: Statistics of thermal plumes and dissipation rates in turbulent Rayleigh-Bénard convection in a cubic cell, *International Journal of Heat and Mass Transfer*, 182, 121 995, <https://doi.org/https://doi.org/10.1016/j.ijheatmasstransfer.2021.121995>, 2022.

Wagner, S., Shishkina, O., and Wagner, C.: Boundary layers and wind in cylindrical Rayleigh-Bénard cells, *Journal of Fluid Mechanics*, 697, 336–366, 2012.

770 Wang, Q., Xia, S.-N., Wang, B.-F., Sun, D.-J., Zhou, Q., and Wan, Z.-H.: Flow reversals in two-dimensional thermal convection in tilted cells, *Journal of Fluid Mechanics*, 849, 355–372, <https://doi.org/10.1017/jfm.2018.451>, 2018.

Wang, Y., He, X., and Tong, P.: Turbulent temperature fluctuations in a closed Rayleigh-Bénard convection cell, *Journal of Fluid Mechanics*, 874, 263–284, <https://doi.org/10.1017/jfm.2019.405>, 2019.

775 Wang, Y., Wei, Y., Tong, P., and He, X.: Collective effect of thermal plumes on temperature fluctuations in a closed Rayleigh-Bénard convection cell, *Journal of Fluid Mechanics*, 934, A13, <https://doi.org/10.1017/jfm.2021.1107>, 2022.

Wei, P.: The persistence of large-scale circulation in Rayleigh-Bénard convection, *Journal of Fluid Mechanics*, 924, A28, <https://doi.org/10.1017/jfm.2021.619>, 2021.

780 Xi, H.-D., Lam, S., and Xia, K.-Q.: From laminar plumes to organized flows: the onset of large-scale circulation in turbulent thermal convection, *Journal of Fluid Mechanics*, 503, 47–56, <https://doi.org/10.1017/S0022112004008079>, 2004.

Xi, H.-D., Zhou, S.-Q., Zhou, Q., Chan, T.-S., and Xia, K.-Q.: Origin of the Temperature Oscillation in Turbulent Thermal Convection, *Phys. Rev. Lett.*, 102, 044 503, <https://doi.org/10.1103/PhysRevLett.102.044503>, 2009.

Xu, A., Chen, X., and Xi, H.-D.: Tristable flow states and reversal of the large-scale circulation in two-dimensional circular convection cells, *Journal of Fluid Mechanics*, 910, A33, <https://doi.org/10.1017/jfm.2020.964>, 2021a.

Xu, W., Wang, Y., He, X., Wang, X., Schumacher, J., Huang, S.-D., and Tong, P.: Mean velocity and temperature profiles in turbulent Rayleigh-Bénard convection at low Prandtl numbers, *Journal of Fluid Mechanics*, 918, A1, <https://doi.org/10.1017/jfm.2021.255>, 2021b.

785 Yan, Z., Li, X., and Yu, C.: Scale locality of helicity cascade in physical space, *Physics of Fluids*, 32, 061 705, <https://doi.org/10.1063/5.0013009>, 2020.

Yano, J.: *Geophysical Convection Dynamics*, no. t. 5 in *Developments in Weather and Climate Science*, Elsevier Science, ISBN 9780323912136, <https://books.google.pl/books?id=bmG9EAAQBAJ>, 2023.

Yano, J.-I. and Morrison, H.: Thermal vortex ring: vortex-dynamics analysis of a high-resolution simulation, *Journal of Fluid Mechanics*, 991, A18, <https://doi.org/10.1017/jfm.2024.485>, 2024.

790 Yao, J. and Hussain, F.: Vortex Reconnection and Turbulence Cascade, *Annual Review of Fluid Mechanics*, 54, 317–347, <https://doi.org/10.1146/annurev-fluid-030121-125143>, 2022.

Zhang, Y.-Z., Sun, C., Bao, Y., and Zhou, Q.: How surface roughness reduces heat transport for small roughness heights in turbulent Rayleigh–Bénard convection, *Journal of Fluid Mechanics*, 836, <https://doi.org/10.1017/jfm.2017.786>, 2018.

795 Zhou, Q. and Xia, K.-Q.: Thermal boundary layer structure in turbulent Rayleigh–Bénard convection in a rectangular cell, *Journal of Fluid Mechanics*, 721, 199–224, <https://doi.org/10.1017/jfm.2013.73>, 2013.

Zhou, S.-Q. and Xia, K.-Q.: Scaling Properties of the Temperature Field in Convective Turbulence, *Phys. Rev. Lett.*, 87, 064501, <https://doi.org/10.1103/PhysRevLett.87.064501>, 2001.

800 Zhou, S.-Q., Xie, Y.-C., Sun, C., and Xia, K.-Q.: Statistical characterization of thermal plumes in turbulent thermal convection, *Phys. Rev. Fluids*, 1, 054301, <https://doi.org/10.1103/PhysRevFluids.1.054301>, 2016.

Zhu, X., Mathai, V., Stevens, R. J. A. M., Verzicco, R., and Lohse, D.: Transition to the Ultimate Regime in Two-Dimensional Rayleigh–Bénard Convection, *Phys. Rev. Lett.*, 120, 144502, <https://doi.org/10.1103/PhysRevLett.120.144502>, 2018.